J. Fluid Mech. (2008), *vol.* 613, *pp.* 275–307.
doi:10.1017/S0022112008003169 Printed in the United Kingdom

Acoustic propagation and scattering in the exhaust flow from coaxial cylinders

B. VEITCH† AND N. PEAKE

Department of Applied Mathmatics & Theoretical Physics, University of Cambridge, Wilberforce Road, Cambridge CB3 0WA, UK

(Received 6 August 2007 and in revised form 24 June 2008)

In this paper we present an analytical solution to the problem of sound radiation from semi-infinite coaxial cylinders, as a model for rearward noise emission by aeroengines. The cylinders carry uniform subsonic flows, whose Mach numbers may differ from each other and from that of the external flow. The incident field takes the form of a downstream-going acoustic mode in either the outer cylinder (the bypass flow) or the inner cylinder (the jet). The key geometrical ingredient of our problem is that the two open ends are staggered by a finite axial distance, so that the inner cylinder can be either buried upstream inside the outer cylinder, or can protrude downstream beyond the end of the outer cylinder (sometimes called the 'half-cowl' configuration). The solution is found by solving a matrix Wiener–Hopf equation, which involves the factorization of a certain matrix $\hat{\boldsymbol{\mathcal{K}}}$ in the form $\hat{\boldsymbol{\mathcal{K}}}^{-}\hat{\boldsymbol{\mathcal{K}}}=\hat{\boldsymbol{\mathcal{K}}}^{+}$, with $\hat{\boldsymbol{\mathcal{K}}}^{\pm}$ analytic, invertible and with algebraic behaviour at infinity in the upper and lower halves of the complex Fourier plane respectively. It turns out that the method of solution is different for the buried and protruding cases. In the buried case the well-known pole removal technique can be applied to a certain meromorphic function (denoted k_{11}), but in the protruding case the corresponding function k_{22} is no longer meromorphic. Progress is made, however, by using a Padé representation of k_{22} to yield a meromorphic problem which can then be solved using the pole removal technique as before. A range of results is presented, for both buried and protruding systems and with and without mean flow, and it becomes clear that the stagger of the two open ends can have a very significant effect on the far-field noise. We also obtain reasonable agreement between our predictions and some experimental results. One particular noise mechanism we identify in the presence of mean shear is the way in which a Kelvin–Helmholtz instability mode launched from the upstream trailing edge can be scattered into sound by its interaction with the downstream edge, provided that the separation between the edges is sufficiently large in a way which we identify.

1. Introduction

Noise emission by large aeroengines is an issue of continued practical interest, and many complex issues concerned with the generation of noise and the way in which it propagates to an observer on the ground or in the aircraft cabin still require considerable attention. One such issue concerns the way in which noise reaches the far field through the rearward arc; noise generated by the fan can propagate along

† Present address: Schlumberger Cambridge Research Ltd., High Cross, Madingley Rise, Cambridge CB3, 0EL, UK.

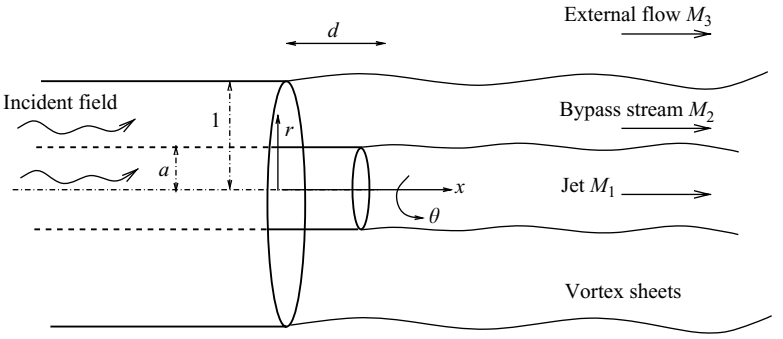

FIGURE 1. The model problem, here in the protruding case $d > 0$ in which the inner pipe protrudes beyond the outer pipe.

the bypass duct, while noise from the aeroengine core propagates through the jet pipe. In both cases the sound is scattered by the trailing edges of the outer cowling and jet nozzle, and is refracted by the non-uniform flow resulting from the mixing of the jet and bypass streams and the atmosphere. The resulting radiation pattern in the far field can be very complex.

In the past a range of simplified model problems have been solved which are relevant to the exhaust noise issue. One of the earliest works was due to Levine & Schwinger (1948), who considered radiation from a semi-infinite cylindrical pipe containing an incident plane wave but with zero mean flow. This was extended to higher-order duct modes and to non-zero mean flow for a leading-edge configuration by Homicz & Lordi (1975). A very important solution was derived by Munt, who considered a semi-infinite hollow cylinder in which the outer and inner uniform mean flows have different Mach numbers (so that the mean flow possesses a vortex sheet), and derived analytical expressions for both the far-field radiation (Munt 1977) and the reflected duct modes (Munt 1990). A low-frequency analysis of Munt's problem has been considered by Cargill (1982*a*, *b*) and Rienstra (1983), and a high-frequency analysis by Cargill (1982*c*). The case of an annular semi-infinite cylinder with equal external, bypass and jet mean-flow Mach numbers was considered by Rienstra (1984); note that even when the mean-flow Mach numbers are equal, scattering of sound still causes unsteady vorticity to be shed from the trailing edges. More recently Gabard & Astley (2006) have extended the Munt solution by including an infinite centrebody. The approach used by all these authors has been to apply the scalar Wiener–Hopf technique (see Noble 1988). This technique allows two unknown functions that are analytic over semi-infinite intervals to be found, effectively the unsteady pressure distribution on the cylinder wall and a corresponding quantity (such as the radial velocity in the fluid) over the semi-infinite extension of the cylinders in the axial direction.

Although the model solutions described in the previous paragraph have proved illuminating, one drawback is that they do not allow for proper representation of a very important feature of the real system, namely that the jet nozzle protrudes a finite distance beyond the end of the nacelle, or in certain configurations is buried a finite distance upstream. Our representation of this situation is shown in figure 1, in which the axial stagger of the two open ends, d, is finite and either positive (the protruding, or sometimes called the 'half-cowl', case as shown in figure 1) or negative (the buried case). In the buried nozzle case Taylor, Crighton & Cargill (1993) derived an approximate solution by splitting the problem up into two semi-infinite geometries which are then solved separately, again by the scalar Wiener–Hopf technique.

However, our aim in this paper is to derive exact solutions, and in order to do this we will need to apply matrix Wiener–Hopf techniques.

In scalar Wiener–Hopf problems one usually makes a multiplicative factorization of a single scalar function. As we will see, the solution of the problem represented in figure 1 results in two coupled Wiener–Hopf problems, which we will write in the form of a matrix equation. The issue then is the multiplicative factorization of the 2×2 matrix $\hat{\mathscr{K}}$ in the form $\hat{\mathscr{K}}^{-}\hat{\mathscr{K}}=\hat{\mathscr{K}}^{+}$, with $\hat{\mathscr{K}}^{+}$ and $\hat{\mathscr{K}}^{-}$ analytic, invertible and with algebraic behaviour at infinity in the upper and lower halves of the complex plane respectively. Unlike the scalar case, there is no general method for completing this factorization, but a number of different techniques are available which work for particular forms of $\hat{\mathscr{K}}$. In one such class of problems, one proceeds by subtracting an infinite series of (unknown) residue contributions in one half-plane from a certain meromorphic function formed from elements of $\hat{\mathscr{K}}$. This leads to an infinite algebraic system for the unknown elements, and the factorization of $\hat{\mathscr{K}}$ is completed by numerical solution of this system. In various guises this approach is the so-called 'weak factorization method' of Idemen (1979) or 'pole removal method' of Abrahams (1987*a*), and many applications of this technique have been made: for instance, by Jones (1986), Abrahams (1987*b*) and Abrahams & Wickham (1988) for the problem of scattering by multiple plane barriers, and recently by Demir & Rienstra (2006) for the problem of radiation from a coaxial cylinder with infinite centrebody in which half of the centre-body has acoustic lining. As we will see, the pole removal method can be applied to the problem shown in figure 1 when $d<0$. In parallel with our current work, Demir & Rienstra (2007) have studied the buried problem using the weak factorization method. Our work, for both the buried nozzle and the protruding nozzle, is reported in Veitch & Peake (2007).

For the protruding case $d>0$ our present problem is not of the form for which the pole removal technique can be applied. However, for a related problem, namely scattering by a pair of staggered plates, Abrahams & Wickham (1988, 1990*b*) have constructed the matrix factorization in terms of the solution of coupled integral equations, which can then be solved iteratively. We could adopt this latter approach here, but instead we prefer to pursue the philosophy developed by Abrahams (1997, 2000), whose idea here is to use Padé approximants (see Baker & Graves-Morris 1996) to approximate a certain complex function (which possesses branch cuts) by a rational function (which is necessarily meromorphic). This has the effect of converting the problem into one in which the pole removal technique described in the previous paragraph can be applied. Abrahams originally developed this idea to transform a class of problems with non-commutative matrix kernels into a generalized Khrapkov form (Khrapkov 1971*a*, *b*; Daniele 1984), and recent applications in elasticity theory have been given by Abrahams (2002) and Owen & Abrahams (2006). Abrahams & Wickham (1990*a*) have presented a method for general Wiener–Hopf matrices containing exponential phase factors (of which our $\hat{\mathscr{K}}$ is an example), with the factors being given in terms of the solution of an integral equation.

In many ways the model problems we seek to solve echo the work of Lawrie, Abrahams & Linton (1993) and Lawrie & Abrahams (1994). These authors considered the acoustic radiation from two opposed semi-infinite cylinders without flow, in the cases in which the cylinders overlap and are separated respectively. In the former case (analogous to our problem with $d<0$) the pole-removal technique is used, while in the latter case (analogous to our problem with $d>0$) an integral equation is derived, which is then solved approximately by Lawrie & Abrahams (1994) in a large-spacing limit. Presumably the latter problem could also be solved using the present Padé method.

The paper is organized as follows. In § 2 we will present the formulation and formal solution of the problem for general d in terms of the unknown factorization of the matrix $\hat{\mathscr{K}}$. In § 3 and § 4 we will present the factorization of $\hat{\mathscr{K}}$ for the buried case $d<0$ and the protruding case $d>0$ respectively, in the former case using the pole removal method directly and in the latter case by first applying a Padé approximation. An approximate solution for $d<0$ is given in § 5, while results for a range of parameter values are given in § 6. Full expressions for the various matrix factors, together with the details of the calculation of certain scalar factors, are presented in Appendices.

2. Model problem

2.1. *Formulation*

We consider the situation shown in figure 1, in which two semi-infinite co-axial cylinders carry uniform axial flows of different speeds emanating from deep inside the cylinders, surrounded by an infinite uniform flow moving at a third speed. In what follows we will non-dimensionalize all lengths by the radius of the outer cylinder, so that the cylinder radii are $a(<1)$ and 1, speeds by the uniform sound speed of the outer flow, and densities by the uniform density of the outer flow. In this way, the uniform flows have non-dimensional velocities M_3 in $r>1$, M_2 in $a<r<1$ and M_1 in $r<a$, where r is the radial coordinate. Similarly the corresponding mean sound speeds and densities are C_j^{-1}, D_j for $j=1,2,3$ respectively, with $C_3=D_3=1$, while the local mean Mach number is M_jC_j. (Note that we use the notation C_j to denote the reciprocal of the dimensionless sound speed, as done by Munt (1977).) We suppose that the flow is subsonic everywhere (supersonic mean flows could be treated, but would require different definitions of various branch cuts in what follows).

The origin of coordinates is taken to be at the centre of the open face of the outer cylinder, with the axial x-direction pointing downstream. The open face of the inner cylinder is displaced by a distance d in the x-direction. In figure 1 the protruding case $d>0$ is shown, but we will also consider the case $d<0$ in which the inner cylinder is buried a distance $-d$ upstream. As we will see, these two cases will require different analysis.

We will consider an incident acoustic field from upstream, located in either $a\leqslant r\leqslant 1$ and corresponding to noise in the bypass duct from the fan, or in $0\leqslant r\leqslant a$ and corresponding to noise from the engine core. For the sake of generality the analysis we present will cover the case of two incident modes of arbitrary amplitudes, one in each region, from which the case of only one incident mode follows simply and the case of multi-mode interaction follows by linear superposition. We consider a single frequency ω throughout (given the choice of normalization this corresponds to the Helmholtz number based on the outer cylinder radius and the sound speed in $r>1$), and also suppose that the incident (and hence the scattered) field possess a single azimuthal mode order m. The time and angular dependence of linear unsteady quantities is therefore expressed in a factor $\exp(-\mathrm{i}\omega t+\mathrm{i}m\theta)$, where θ is the polar angle. The incident field interacts with the ends of the two cylinders and with the vortex sheets to produce a scattered field. We will denote the velocity potential for the incident field in the bypass and the core as $\phi_{inc}^{b,c}(x,r)\exp(-\mathrm{i}\omega t+\mathrm{i}m\theta)$ respectively. In what follows superfixes b,c will refer to the regions $a\leqslant r\leqslant 1$ (bypass) and $r\leqslant a$ (core) respectively. The potential of the total unsteady field, $\phi_t(x,r)\exp(-\mathrm{i}\omega t+\mathrm{i}m\theta)$, can then be written in terms of the scattered potential $\phi(x,r)\exp(-\mathrm{i}\omega t+\mathrm{i}m\theta)$,

with

$$\phi_t = \begin{cases} \phi & (r \geqslant 1), \\ \phi + \phi^b_{inc} & (a \leqslant r \leqslant 1), \\ \phi + \phi^c_{inc} & (0 \leqslant r \leqslant a). \end{cases} \tag{2.1}$$

All of the potentials satisfy the convected form of the Helmholtz equation

$$C_j^2 \left(-\mathrm{i}\omega + M_j \frac{\partial}{\partial x} \right)^2 \phi = \nabla^2 \phi \ , \qquad j = 1, 2, 3, \tag{2.2}$$

in the corresponding portion of the flow, while the unsteady scattered pressure is given by

$$p(x, r) = D_j \left[\mathrm{i}\omega\phi - M_j \frac{\partial \phi}{\partial x} \right]. \tag{2.3}$$

The corresponding density fluctuation follows from $\rho = C_j^2 p$.

Throughout this paper we will take the walls of the cylinders to be rigid, so that the wall-normal velocity is zero. By considering for the moment each cylinder to be infinitely long and then taking the axial Fourier transform, defined by

$$\Phi(\alpha, r) = \int_{-\infty}^{\infty} \phi(x, r) \exp(\mathrm{i}\alpha x) \mathrm{d}x, \tag{2.4}$$

of (2.2), it is a straightforward matter to find the incident fields in the form

$$\left.\begin{aligned} \phi^b_{inc} &= k^b \big[-\mathrm{K}'_m\big(\gamma_2\big(\alpha^{b,-}_{inc}\big)\big)\mathrm{I}_m\big(\gamma_2\big(\alpha_{inc}{}^{b,-}\big)r\big) \\ &\qquad + \mathrm{I}'_m\big(\gamma_2\big(\alpha^{b,-}_{inc}\big)\big)\mathrm{K}_m\big(\gamma_2\big(\alpha^{b,-}_{inc}\big)r\big)\big] \exp\big(-\mathrm{i}\alpha^{b,-}_{inc} x\big), \\ \phi^c_{inc} &= k^c \mathrm{I}_m\big(\gamma_1\big(\alpha^{c,-}_{inc}\big)r\big) \exp\big(-\mathrm{i}\alpha^{c,-}_{inc} x\big). \end{aligned}\right\} \tag{2.5}$$

Here I_m and K_m are modified Bessel functions of order m, the axial eigenvalue $\alpha^{c,-}_{inc}$ corresponds to one of the finite number of downstream-propagating solutions of the dispersion relation in $r \leqslant a$,

$$\mathrm{I}'_m(\gamma_1(\alpha)a) = 0, \tag{2.6}$$

where the superfix $-$ indicates that the mode is located in the lower half of the complex α-plane. Similarly, the axial eigenvalue $\alpha^{b,-}_{inc}$ corresponds to one of the finite number of downstream-propagating solutions of the dispersion relation in $a \leqslant r \leqslant 1$,

$$\Delta \equiv \mathrm{I}'_m(\gamma_2(\alpha)a)\mathrm{K}'_m(\gamma_2(\alpha)) - \mathrm{K}'_m(\gamma_2(\alpha)a)\mathrm{I}'_m(\gamma_2(\alpha)) = 0. \tag{2.7}$$

The functions $\gamma_j(\alpha)$ for $j = 1, 2, 3$ are defined in the complex α-plane via

$$\gamma_j^2(\alpha) = \beta_j^2 \left[\alpha - \frac{\omega C_j}{1 - M_j C_j} \right] \left[\alpha + \frac{\omega C_j}{1 + M_j C_j} \right], \tag{2.8}$$

where $\beta_j^2 = 1 - M_j^2 C_j^2$, with branch cuts joining the branch points $\pm\omega C_j/(1 \mp M_j C_j)$ to infinity through the upper and lower half-planes respectively, and with $\gamma_j(\alpha)$ real and positive as α approaches infinity along the positive real axis. In (2.5) the constant factors $k^{c,b}$ are chosen to be either zero if that incident mode is not being considered, or so as to scale the amplitude of the mode in some suitable way (typically in this paper so that the total incident dimensionless power is unity).

Finally, we note in this subsection that the boundary conditions to be satisfied are that the total normal velocity is zero on all walls, and that the total particle displacement and the total pressure are continuous across the vortex sheets. At the

cylinder trailing edges we will impose the full unsteady Kutta condition, Crighton (1985). This condition ensures that the flow is smooth near the trailing edge; in particular the unsteady pressure necessarily remains finite, and the vortex sheet deflection varies in proportion to distance from the edge to the 3/2 power, so that the vortex sheet remains parallel to the wall at the edge.

We also require all solutions to be causal, and therefore composed of out-going waves at infinity. The application of causality in problems involving vortex sheets requires care, and has received a great deal of attention. We mention in particular here the work of Crighton & Leppington (1974), who obtained a causal solution to the problem of excitation of a vortex sheet by rotating their temporal inversion in the complex ω-plane. We will not repeat their arguments here, but note that (with one exception) we can simply suppose that in our problem ω has a small positive imaginary part, and that the complex α-plane be divided into the upper and lower half-planes which overlap in a vanishingly thin strip containing the real axis. Modes whose wavenumbers are complex for real ω then lie in the corresponding half-plane, while neutral downstream/upstream modes (on the real α axis for real ω) are assigned to the upper/lower half-planes respectively. The exception comes from the Kelvin–Helmholtz instability modes of the vortex sheets, which although having $\mathrm{Im}(\alpha) > 0$ for real ω must be treated as being in the lower half-α-plane. This latter point ensures that when the Fourier transform is inverted for $x > 0$ by closing in the lower half-plane, the contribution from the Kelvin–Helmholtz mode is picked up as a convective instability.

2.2. *Fundamental equation*

We now present the formal solution to the problem described in the previous subsection. The first step is to take the Fourier transform of (2.2) with respect to x. This leads to a second-order ordinary differential equation in r, and by solving this equation and imposing regularity conditions on the axis and at infinity, it follows that

$$\Phi(\alpha, r) = \begin{cases} A\mathrm{I}_m(\gamma_1 r) & (r \leqslant a), \\ B\mathrm{I}_m(\gamma_2 r) + C\mathrm{K}_m(\gamma_2 r) & (a \leqslant r \leqslant 1), \\ D\mathrm{K}_m(\gamma_3 r) & (r \geqslant 1), \end{cases} \tag{2.9}$$

where A, B, C, D are as yet unknown functions of α.

Turning first to the conditions across $r = 1$, the rigid wall condition in $x < 0$ implies that

$$\frac{\partial \Phi^-}{\partial r}(\alpha, 1-) = \frac{\partial \Phi^-}{\partial r}(\alpha, 1+) = 0, \tag{2.10}$$

while continuity of particle displacement across the vortex sheet in $x > 0$ implies that

$$(\omega + \alpha M_3)\frac{\partial \Phi^+}{\partial r}(\alpha, 1-) = (\omega + \alpha M_2)\frac{\partial \Phi^+}{\partial r}(\alpha, 1+). \tag{2.11}$$

Here the superfixes $\pm$ denote the half-range Fourier transforms along the positive and negative real x-axes respectively, and imply that the corresponding functions are analytic in the upper and lower halves of the complex α-plane respectively. The continuity of total unsteady pressure across the vortex sheet $r = 1, x > 0$ leads to

$$(\omega + \alpha M_3)\Phi^+(\alpha, 1+) - D_2(\omega + \alpha M_2)\Phi^+(\alpha, 1-) - \mathrm{i}M_3\phi(0, 1+) + \mathrm{i}D_2 M_2\phi(0, 1-) = F_-^+ \equiv \frac{f}{\alpha - \alpha_{inc}^{b,-}}, \tag{2.12}$$

where now $\Phi^+(\alpha, r)$ is the half-range Fourier transform of $\phi(x, r)$ over $x > 0$. The constant f, which arises from the pressure of the incident bypass mode on $r = 1-$, is

$$f = \frac{\mathrm{i}k^b D_2\left(\omega + \alpha_{inc}^{b,-} M_2\right)}{\gamma_2\left(\alpha_{inc}^{b,-}\right)}. \tag{2.13}$$

Note that the left-hand side of (2.12) is analytic in the upper half of the α-plane, a fact confirmed on the right-hand side by the fact that the pole at the incident wavenumber $\alpha = \alpha_{inc}^{b,-}$ lies in the lower half-plane.

Turning now to the conditions across $r = a$, we first note that we can decompose the full-range Fourier transform by writing

$$\begin{aligned}\frac{\partial \Phi}{\partial r}(\alpha, r) &= \int_d^\infty \frac{\partial \phi}{\partial r} \exp(\mathrm{i}\alpha x)\mathrm{d}x + \int_{-\infty}^d \frac{\partial \phi}{\partial r} \exp(\mathrm{i}\alpha x)\,\mathrm{d}x \\ &= \exp(\mathrm{i}\alpha d) \int_0^\infty \frac{\partial \phi}{\partial r} \exp(\mathrm{i}\alpha x')\mathrm{d}x' + \exp(\mathrm{i}\alpha d) \int_{-\infty}^0 \frac{\partial \phi}{\partial r} \exp(\mathrm{i}\alpha x')\,\mathrm{d}x' \\ &\equiv \exp(\mathrm{i}\alpha d)\left[\frac{\partial \Phi^+}{\partial r}(\alpha, r) + \frac{\partial \Phi^-}{\partial r}(\alpha, r)\right]. \end{aligned} \tag{2.14}$$

Note again that the $\pm$ superfixes in the last line correspond to functions which are analytic in the upper and lower halves of the complex α-plane. The hard-wall condition on $r = a, x < d$ implies

$$\frac{\partial \Phi^-}{\partial r}(\alpha, a-) = \frac{\partial \Phi^-}{\partial r}(\alpha, a+) = 0, \tag{2.15}$$

while the continuity of particle displacement across $r = a, x > d$ gives

$$(\omega + \alpha M_2)\frac{\partial \Phi^+}{\partial r}(\alpha, a-) = (\omega + \alpha M_1)\frac{\partial \Phi^+}{\partial r}(\alpha, a+). \tag{2.16}$$

Finally, the continuity of pressure condition across the vortex sheet $r = a, x > d$ yields

$$\begin{aligned}-D_2(\omega + \alpha M_2)\Phi^+(\alpha, a+) + D_1(\omega + \alpha M_1)\Phi^+(\alpha, a-) + \mathrm{i}D_2 M_2 \phi(d, a+) \\ - \mathrm{i}D_1 M_1 \phi(d, a-) = \frac{g}{\alpha - \alpha_{inc}^{b,-}} + \frac{h}{\alpha - \alpha_{inc}^{c,-}} \equiv G^+, \end{aligned} \tag{2.17}$$

where the constants g, h arise from the pressure of the incident bypass and core modes on $r = a$ and are given by

$$\left.\begin{aligned} g &= \mathrm{i}k^b D_2\left(\omega + \alpha_{inc}^{b,-} M_2\right)\left[\mathrm{K}_m\left(\gamma_2\left(\alpha_{inc}^{b,-} a\right)\right)\mathrm{I}'_m\left(\gamma_2\left(\alpha_{inc}^{b,-}\right)\right)\right. \\ &\quad \left. -\mathrm{K}'_m\left(\gamma_2\left(\alpha_{inc}^{b,-}\right)\right)\mathrm{I}_m\left(\gamma_2\left(\alpha_{inc}^{b,-} a\right)\right)\right] \exp\left(-\mathrm{i}\alpha_{inc}^{b,-} d\right), \\ h &= -\mathrm{i}k^c D_1 \mathrm{I}_m\left(\gamma_1\left(\alpha_{inc}^{c,-} a\right)\right)\left(\omega + \alpha_{inc}^{c,-} M_1\right) \exp\left(-\mathrm{i}\alpha_{inc}^{c,-} d\right). \end{aligned}\right\} \tag{2.18}$$

We now substitute equation (2.9) into equations (2.10)–(2.18), and upon eliminating A, B, C, D and after a great deal of algebra we arrive at the matrix equation

$$\mathscr{K} \boldsymbol{\Phi}_r^+ = \boldsymbol{F}^+ + \boldsymbol{\Psi}^-. \tag{2.19}$$

Here the vector $\boldsymbol{\Phi}_r^+ = [\partial \Phi^+(\alpha, a+)/\partial r, \partial \Phi^+(\alpha, 1-)/\partial r]$, i.e. the transforms of the normal velocities on the vortex sheets, and is analytic in the upper half-plane. The

vector $\boldsymbol{\Psi}^-$, given by

$$\begin{pmatrix} -D_2(\omega+\alpha M_2)\Phi^-(\alpha,a+) + D_1(\omega+\alpha M_1)\Phi^-(\alpha,a-) - \mathrm{i}D_2M_2\phi(d,a+) + \mathrm{i}D_1M_1\phi(d,a-) \\ (\omega+\alpha M_3)\Phi^-(\alpha,1+) - D_2(\omega+\alpha M_2)\Phi^-(\alpha,1-) + \mathrm{i}M_3\phi(0,1+) - \mathrm{i}D_2M_2\phi(0,1-) \end{pmatrix}, \tag{2.20}$$

is related to the unsteady scattered pressure jumps across the cylinder walls, and is analytic in the lower half-plane. Finally, the vector $\boldsymbol{F}^+ = [G^+, F^+]$ is analytic in the upper half-plane, and is related to the forcing provided by the pressure jump of the incident field across the cylinder walls. The 2×2 matrix $\mathscr{K}$ is given by

$$\mathscr{K} = \frac{1}{(\omega+\alpha M_2)\Delta\gamma_2} \begin{pmatrix} k_{11} & k_{12}\exp(-\mathrm{i}\alpha d) \\ k_{21}\exp(\mathrm{i}\alpha d) & k_{22} \end{pmatrix}, \tag{2.21}$$

where

$$\left.\begin{aligned} k_{12} &= -\frac{D_2(\omega+\alpha M_2)^2}{a\gamma_2}, \qquad k_{21} = \frac{D_2(\omega+\alpha M_2)^2}{\gamma_2}, \\ k_{11} &= \frac{D_1(\omega+\alpha M_1)^2\gamma_2 \mathrm{I}_m(\gamma_1 a)\Delta}{\gamma_1 \mathrm{I}'_m(\gamma_1 a)} + D_2(\omega+\alpha M_2)^2[\mathrm{K}_m(\gamma_2 a)\mathrm{I}'_m(\gamma_2) - \mathrm{I}_m(\gamma_2 a)\mathrm{K}'_m(\gamma_2)], \\ k_{22} &= \frac{(\omega+\alpha M_3)^2\gamma_2 \mathrm{K}_m(\gamma_3)\Delta}{\gamma_3 \mathrm{K}'_m(\gamma_3)} + D_2(\omega+\alpha M_2)^2[\mathrm{K}'_m(\gamma_2 a)\mathrm{I}_m(\gamma_2) - \mathrm{K}_m(\gamma_2)\mathrm{I}'_m(\gamma_2 a)], \end{aligned}\right\} \tag{2.22}$$

and Δ has already been defined in (2.7). Note that the dependence of $\mathscr{K}$ on the stagger d occurs only through the exponential phase factors $\exp(\pm\mathrm{i}\alpha d)$ in the off-diagonal elements in (2.21), so that k_{11}, k_{12}, k_{21}, k_{22} are independent of d.

Equation (2.19) is the fundamental equation to be solved in this paper, and this will be accomplished using the Wiener–Hopf technique. Before presenting the formal solution, however, we will first consider the properties of some of the quantities in (2.21), (2.22) in more detail.

2.3. *Various dispersion relations*

The functions $k_{11}(\alpha)$ and $k_{22}(\alpha)$ will prove to be very important in our subsequent calculations. In particular, the equation $k_{11} = 0$ corresponds to the dispersion relation for fluid contained within an infinitely long hard-walled cylinder of radius 1 carrying mean flow of speed M_2 in $a \leqslant r \leqslant 1$ and speed M_1 in $0 \leqslant r \leqslant a$. This system is of course relevant to the case of a buried nozzle $d < 0$ in the region $d < x < 0$. On the other hand, the equation $k_{22} = 0$ is the dispersion relation for a fluid outside an infinite rigid cylinder $r = a$ with mean flow of speed M_2 in $a \leqslant r \leqslant 1$ and speed M_3 in $1 \leqslant r < \infty$. This second system is relevant to the case $d > 0$ in the region $0 < x < d$. In what follows we will be required to factorize the matrix $\hat{\mathscr{K}}$, and invert the factors, and we will therefore also be concerned with the zeros of the quantity $k_{11}k_{22} - k_{21}k_{12}$, which is proportional to the determinant of $\mathscr{K}$. It is straightforward but tedious to show that $\det\mathscr{K}$ is proportional to Δ.

The locations of some of the zeros of Δ, k_{11} and $\det(\mathscr{K})$ in the α-plane are shown in figure 2. The zeros of Δ are the acoustic modes in the outer cylinder; in figure 2 there is one real mode propagating upstream and one propagating downstream, i.e. the wavenumbers $\alpha = \alpha_{inc}^{b,\pm}$ respectively, and an infinite number of evanescent modes which approach infinity along $\mathrm{Re}(\alpha) = \omega C_2^2 M_2/(1 - C_2^2 M_2^2)$. The function k_{11}

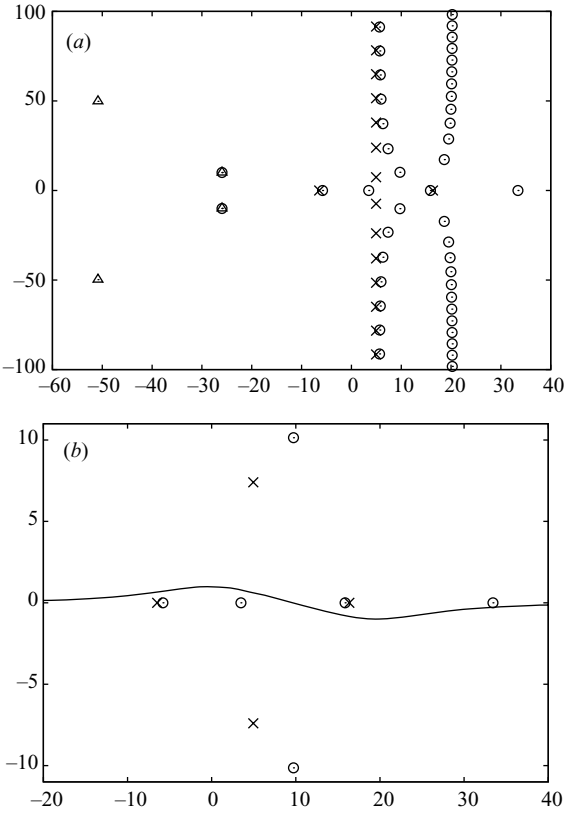

FIGURE 2. In the complex α-plane the zeros of k_{11} (open circle symbols) and the dispersion function in the outer duct Δ (multiplication symbols). Also plotted are the two sets of Kelvin–Helmholtz modes of $(\det\mathscr{K})/\Delta$ (triangle symbols). The parameter values are $\omega = 15$, $m = 4$, $a = 0.75$, $M_1 = 0.7$, $M_2 = 0.3$, $M_3 = 0$ and for a cold jet, i.e. $D_j = C_j = 1$ for $j = 1, 2$. (b) A close-up view of (a), in which is also plotted (solid line) a typical integration contour C (see Appendix A).

also possesses a finite number of real zeros; in figure 2, two of these real modes correspond to waves propagating in the downstream direction, and two correspond to waves propagating upstream. The evanescent modes of $k_{11} = 0$ approach infinity along the vertical asymptotes $\mathrm{Re}(\alpha) = \omega C_{1,2}^2 M_{1,2}/1 - C_{1,2}^2 M_{1,2}^2$. As well as all these acoustic modes, k_{11} possesses a pair of complex-conjugate modes, w_0, w_0^*, which correspond to the Kelvin–Helmholtz modes of the cylindrical vortex sheet $r = a$ within the duct $r = 1$. (In figure 2, $w_0 = -25.97 + 10.03\mathrm{i}$, and is virtually coincident with a mode of $\det\mathscr{K}$.) As already noted, despite its location w_0 must be taken to lie in the lower half-plane.

The function $(\det\mathscr{K})/\Delta$ possesses two pairs of complex-conjugate roots u_0, u_0^*, v_0, v_0^* (with in this case $v_0 = -25.97 + 10.03\mathrm{i}$, $u_0 = -50.86 + 49.76\mathrm{i}$). The root v_0 can be associated with the Kelvin–Helmholtz instability of a vortex sheet $r = a$, and indeed is indistinguishable from the instability mode w_0 of k_{11}, while the root u_0 is associated with the vortex sheet $r = 1$, and is indistinguishable from the corresponding zero of k_{22}. The function $(\det\mathscr{K})/\Delta$ possesses a number of acoustic modes (some of them real), which have not been plotted here.

2.4. *Formal expressions for the acoustic field*

We now present the formal solution of (2.19). We first introduce a new matrix $\hat{\mathscr{K}}$ via $\mathscr{K} = \hat{\mathscr{K}}\mathscr{D}^+$, where

$$\mathscr{D}^+ = \begin{pmatrix} (\alpha - v_0)(\alpha - v_0^*) & 0 \\ 0 & (\alpha - u_0)(\alpha - u_0^*) \end{pmatrix}, \tag{2.23}$$

and u_0, v_0 are the Kelvin–Helmholtz instability modes of $\det\mathscr{K}$ described in the previous subsection. The reason for explicitly factorizing out the modes in this way is that it will be much easier to account for the fact that they must all be included in the lower half of the α-plane. In fact, the matrix $\mathscr{D}^+$ has a $+$ superfix to denote the fact that it is non-singular in the upper half-plane. We proceed by factorizing the matrix $\hat{\mathscr{K}}$ in the form

$$\hat{\mathscr{K}}^-\hat{\mathscr{K}} = \hat{\mathscr{K}}^+, \tag{2.24}$$

where the matrices $\hat{\mathscr{K}}^\pm$ are analytic, invertible and have algebraic behaviour at infinity in the upper and lower half-planes respectively. These factors certainly exist under quite general conditions (see Noble 1988, p. 157 and the references contained therein), but no factorization method exists for general Wiener–Hopf problems, and each problem must be approached on a case by case basis. The determination of these factors for our problem will be described later. Now substituting (2.24) into (2.19) and premultiplying by $\hat{\mathscr{K}}^-$ we find that

$$\hat{\mathscr{K}}^+\mathscr{D}^+\boldsymbol{\Phi}_r^+ = \hat{\mathscr{K}}^-\boldsymbol{\Psi}^- + \boldsymbol{E}, \tag{2.25}$$

where $\boldsymbol{E}(\alpha) \equiv \hat{\mathscr{K}}^-\boldsymbol{F}^+$.

The term on the left and the first term on the right of (2.25) are analytic in the upper and lower half-planes respectively. Noting that the singularities in $\boldsymbol{F}^+(\alpha)$ occur only at the two poles $\alpha = \alpha_{inc}^{b,-}, \alpha_{inc}^{c,-}$ in the lower half-plane, it is a simple matter to separate off these two singularities explicitly to write $\boldsymbol{E} = \boldsymbol{E}^+ + \boldsymbol{E}^-$, where

$$\boldsymbol{E}^+(\alpha) = \hat{\mathscr{K}}^-\big(\alpha_{inc}^{b,-}\big)\begin{pmatrix} \dfrac{g}{\alpha - \alpha_{inc}^{b,-}} \\ \dfrac{f}{\alpha - \alpha_{inc}^{b,-}} \end{pmatrix} + \hat{\mathscr{K}}^-\big(\alpha_{inc}^{c,-}\big)\begin{pmatrix} \dfrac{h}{\alpha - \alpha_{inc}^{c,-}} \\ 0 \end{pmatrix} \tag{2.26}$$

is analytic in the upper half-plane. The vector $\boldsymbol{E}^-(\alpha)$ can be obtained by subtracting (2.26) from the definition of $\boldsymbol{E}(\alpha)$, and is analytic in the lower half-plane. We can now rearrange (2.25) to arrive at the Wiener–Hopf matrix equation

$$-\boldsymbol{E}^+ + \hat{\mathscr{K}}^+\mathscr{D}^+\boldsymbol{\Phi}_r^+ = \hat{\mathscr{K}}^-\boldsymbol{\Psi}^- + \boldsymbol{E}^-. \tag{2.27}$$

Now note that the left-hand side of (2.27) is analytic in the upper half-plane and the right-hand side is analytic in the lower half-plane. The final step in the analysis is to consider the behaviour of the terms in (2.27) at infinity. We will show in Appendix A that in general the elements of $\hat{\mathscr{K}}^+$ approach infinity in the upper half-plane proportionally to $\alpha^{-3/2}$, while the elements of $\hat{\mathscr{K}}^-$ approach infinity in the lower half-plane proportionally to $\alpha^{1/2}$. Further, the unsteady Kutta condition tells us that close to the trailing edge the vortex sheet displacement is proportional to distance from the trailing edge to the power 3/2. The half-range transform of the continuity of particle displacement across the vortex sheets can then be used to show that $\boldsymbol{\Phi}_r^+ \sim \alpha^{-3/2}$ as α goes to infinity in the upper half-plane. It is a straightforward

matter to show that $\boldsymbol{E}^+ \sim \alpha^{-1}$ and $\boldsymbol{E}^- \sim \alpha^{-1/2}$ at infinity in the corresponding half-planes. Putting all this together, we see that the left/right-hand sides of (2.27) define functions which are analytic in the upper/lower halves of the complex α-plane, so that by analytic continuation we can define an entire function. This entire function approaches zero at infinity in both the upper and lower half-planes, and by Liouville's Theorem it therefore follows that the entire function, and hence both sides of (2.27), are identically zero. This leads to, for instance,

$$\boldsymbol{\Phi}_r^+ = (\mathscr{D}^+)^{-1}(\hat{\mathscr{K}}^+)^{-1}\boldsymbol{E}^+. \tag{2.28}$$

From this result the original unknown quantities A, B, C, D in equation (2.9) can be recovered, and the solution of the problem therefore found.

2.5. *Calculation of the far-field acoustic pressure*

In this paper we will be mainly concerned with the acoustic far field generated by the scattering of the incident modes. We therefore consider first the region $r \geqslant 1$, in which the pressure can be recovered by inverting the corresponding Fourier transform in (2.9). This leads to

$$p = \frac{\mathrm{i}}{2\pi}\int_C \frac{(\omega + M_3\alpha)^2\Phi_r^+(\alpha, 1-)\mathrm{K}_m(\gamma_3 r)\exp(-\mathrm{i}\alpha x)}{(\omega + M_2\alpha)\gamma_3\mathrm{K}_m'(\gamma_3)}\mathrm{d}\alpha, \tag{2.29}$$

where $\Phi_r^+(\alpha, 1-)$ can be taken from the formal solution (2.28). The inversion contour C is the real axis suitably deformed to lie above/below all modes in the lower/upper half-plane, as shown in figure 2. Now taking the limit $r \to \infty$, we can use the large-argument form of $\mathrm{K}_m(\gamma_3 r)$ (Abramowitz & Stegun 1965, p. 378) to yield the far-field result

$$p \sim \frac{\mathrm{i}}{\sqrt{8\pi}}\int_C \frac{(\omega + M_3\alpha)^2\Phi_r^+(\alpha, 1-)\exp(-Rf)}{(\omega + M_2\alpha)\mathrm{K}_m'(\gamma_3)\sqrt{\gamma_3^3 r}}\mathrm{d}\alpha, \tag{2.30}$$

where $f(\alpha) = \gamma_3 \sin\Theta + \mathrm{i}\alpha\cos\Theta$, the angle between the downstream x-axis and the observer location is Θ, and $R = \sqrt{r^2 + x^2}$ is the observer distance. We now proceed by using the method of steepest descents: the single saddle point of $f(\alpha)$ is found to be

$$\alpha_s = \frac{M_3\omega - \dfrac{\omega\cos\Theta}{\sqrt{1 - M_3^2\sin^2\Theta}}}{1 - M_3^2}; \tag{2.31}$$

the integration contour C is then deformed onto the steepest descent contour passing through α_s, picking up possible residue contributions from the Kelvin–Helmholtz modes; and the integral along the steepest descent contour can then be evaluated asymptotically in the limit $R \to \infty$ to give the final result. The Kelvin–Helmholtz instability contributes to the hydrodynamic field, while the saddle-point contribution alone can be identified with the acoustic field in $r > 1$. We consider just the acoustic pressure here, which has the far-field form

$$p \sim \frac{D(\Theta)}{R}\exp\left[-\frac{\mathrm{i}M_3\omega R\cos\theta}{1 - M_3^2} + \frac{\mathrm{i}\omega R\sqrt{1 - M_3^2\sin^2\Theta}}{1 - M_3^2}\right], \tag{2.32}$$

where the pressure directivity $D(\theta)$ is given by

$$D(\Theta) = \frac{(\omega + M_3\alpha_s)^2 \Phi_r^+(\alpha_s, 1-)}{2(\omega + M_2\alpha_s)\omega \mathrm{K}'_m(\gamma_3(\alpha_s)) \sin\Theta}. \tag{2.33}$$

Note that in (2.33) there is in fact no singularity when $\sin\Theta = 0$, because $\gamma_3(\alpha_s) \propto \sin\Theta$ and the term in the denominator $\mathrm{K}'_m(\gamma_3(\alpha_s)) \propto (\sin\Theta)^{-m-1}$ as $\sin\Theta \to 0$.

2.6. *Calculation of the acoustic pressure in the duct*

As well as the far-field radiation we will also be interested in the reflected field inside the bypass duct and jet pipe. Turning first to the bypass duct, $a \leqslant r \leqslant 1$, $x < \min(0, d)$, it is easy to show that the scattered potential takes the form

$$\phi = \mathrm{i} \sum_{i=1}^{\infty} \left[B_i \mathrm{I}_m\left(\gamma_2\left(\alpha_i^{b,+}\right) r\right) + C_i \mathrm{K}_m\left(\gamma_2\left(\alpha_i^{b,+}\right) r\right) \right] \exp\left(-\mathrm{i}\alpha_i^{b,+} x\right), \tag{2.34}$$

where the summation is over all wavenumber solutions $\alpha_i^{b,+}$ of the bypass dispersion relation (2.7) in the upper half-plane. The coefficients B_i, C_i are given by

$$\begin{pmatrix} B_i \\ C_i \end{pmatrix} = \frac{\exp\left(\mathrm{i}\alpha_i^{b,+} d\right) \mathfrak{r}_\mathrm{i}}{\gamma_2\left(\alpha_i^{b,+}\right)} \begin{pmatrix} \mathrm{K}'_m\left(\gamma_2\left(\alpha_i^{b,+}\right)\right) & -\exp\left(-\mathrm{i}\alpha_i^{b,+} d\right) \mathrm{K}'_m\left(a\gamma_2\left(\alpha_i^{b,+}\right)\right) \\ -\mathrm{I}'_m\left(\gamma_2\left(\alpha_i^{b,+}\right)\right) & +\exp\left(-\mathrm{i}\alpha_i^{b,+} d\right) \mathrm{I}'_m\left(a\gamma_2\left(\alpha_i^{b,+}\right)\right) \end{pmatrix} \times \left\{ (\mathscr{D})^{-1} (\hat{\boldsymbol{\mathscr{K}}}^+)^{-1} \boldsymbol{E}^+ \right\}\left(\alpha_i^{b,+}\right), \tag{2.35}$$

where $\mathfrak{r}_\mathrm{i}$ is the residue of $1/\Delta$ at $\alpha = \alpha_i^{b,+}$, and the notation $\{...\}(\alpha_i^{b,+})$ indicates that the whole of the matrix-vector product has been evaluated at $\alpha = \alpha_i^{b,+}$.

In the jet pipe $0 \leqslant r \leqslant a$, $x < d$ the scattered potential takes the form

$$\phi = \mathrm{i} \sum_{i=1}^{\infty} A_i \mathrm{I}_m\left(\gamma_1\left(\alpha_i^{c,+}\right) r\right) \exp\left(-\mathrm{i}\alpha_i^{c,+} x\right), \tag{2.36}$$

where the summation is over all wavenumber solutions $\alpha_i^{c,+}$ of the jet dispersion relation (2.6) in the upper half-plane. The coefficients A_i are given by

$$A_i = \frac{\exp\left(\mathrm{i}\alpha_i^{c,+} d\right) \mathfrak{s}_\mathrm{i}}{\gamma_2\left(\alpha_i^{c,+}\right)} \left\{ (\mathscr{D})^{-1} (\hat{\boldsymbol{\mathscr{K}}}^+)^{-1} \boldsymbol{E}^+ \right\}_1 \left(\alpha_i^{c,+}\right), \tag{2.37}$$

where $\mathfrak{s}_\mathrm{i}$ is the residue of $1/\mathrm{I}'_m(\gamma_1 a)$ at $\alpha = \alpha_i^{c,+}$, and the suffix 1 refers to the first component of the vector.

In due course we will use the results in this subsection to help validate our results and to make some absolute-level predictions with experimental data.

3. Factorization of $\hat{\mathscr{K}}$ for a buried nozzle

In the buried nozzle configuration $d < 0$ it turns out that the matrix factorization of $\hat{\mathscr{K}}$ in the form given by (2.24) can be carried out using the pole removal technique (Idemen 1979; Abrahams 1987*a*). We write

$$\hat{\mathscr{K}}^\pm = \begin{pmatrix} \hat{k}_{11}^\pm & \hat{k}_{12}^\pm \\ \hat{k}_{21}^\pm & \hat{k}_{22}^\pm \end{pmatrix}. \tag{3.1}$$

Equating the 1,1 elements in (2.24) and rearranging then yields

$$\hat{k}_{11}^{+}L^{+} = \frac{\hat{k}_{11}^{-}}{L^{-}} + \frac{\hat{k}_{12}^{-}k_{21}}{k_{11}L^{-}}\exp(\mathrm{i}\alpha d), \tag{3.2}$$

where the scalar kernel $L(\alpha)$, given by

$$L = (\omega + \alpha M_2)\gamma_2 \Delta(\alpha - v_0)(\alpha - v_0^*)/k_{11}, \tag{3.3}$$

has been factorized in the form $L(\alpha) = L^{+}(\alpha)L^{-}(\alpha)$, with $L^{\pm}(\alpha)$ analytic and non-zero and with algebraic behaviour at infinity in the upper and lower halves of the complex α-plane respectively. We now note that the left-hand side of (3.2) is analytic in the upper half-plane, but that the right-hand side is not, thanks to the presence of the factor k_{21}/k_{11}. However, the crucial point now is that k_{21}/k_{11} is a meromorphic function, with an infinite number of poles at the zeros of k_{11}. We subtract off the residue ccontributions at each of these poles lying in the lower half-plane (call them β_i^- for $i = 1, 2, ...$, but note that in this notation they, and the β_i^+ which follow, have a superfix, and are not to be confused with the Prandtl–Glauert factors $\beta_{1,2,3}$), and then rearranging (3.2) we find that

$$\begin{aligned}\hat{k}_{11}^{+}(\alpha)L^{+}(\alpha) - \sum_{i=1}^{\infty} \frac{\hat{k}_{12}^{-}(\beta_i^-)R_i \exp(\mathrm{i}\beta_i^- d)}{L^{-}(\beta_i^-)(\alpha - \beta_i^-)} \\ = \frac{\hat{k}_{11}^{-}(\alpha)}{L^{-}} + \left\{ \frac{\hat{k}_{12}^{-}(\alpha)k_{21}(\alpha)}{k_{11}(\alpha)L^{-}(\alpha)}\exp(\mathrm{i}\alpha d) - \sum_{i=1}^{\infty} \frac{\hat{k}_{12}^{-}(\beta_i^-)R_i \exp(\mathrm{i}\beta_i d)}{L^{-}(\beta_i^-)(\alpha - \beta_i^-)} \right\}.\end{aligned} \tag{3.4}$$

Here R_i is the residue of k_{21}/k_{11} at $\alpha = \beta_i^-$. We now note that the left of (3.4) is analytic in the upper half-plane, while the right-hand side is analytic in the lower half-plane. Note also that since $d < 0$ the term $\exp(\mathrm{i}\alpha d)$ on the right decays exponentially in the lower half-plane, allowing both sides of the equation to have algebraic behaviour at infinity in the appropriate half-plane. We therefore have an entire function defined in the whole of the α-plane via (3.4), and application of the extended form of Liouville's Theorem then implies that this entire function is a constant. In fact, we have freedom to choose the value of this constant (corresponding to the non-uniqueness of the factorization (2.24)), and for definiteness and simplicity we therefore choose the entire function to be identically unity.

The calculation in the previous paragraph has given us an expression for the unknown function $\hat{k}_{11}^{+}(\alpha)$ and a relationship between the unknown functions $\hat{k}_{11}^{-}(\alpha)$ and $\hat{k}_{12}^{-}(\alpha)$, both in terms of the unknown $\hat{k}_{12}^{-}(\beta_i^-)$, and these are given in Appendix B as equations (B 1) and (B 5). We now derive more such relationships by eliminating $\hat{k}_{11}^{-}$ between the equations resulting from equating the 1,1 and 1,2 elements in (2.24). After some algebra we arrive at

$$\begin{aligned}\hat{k}_{12}^{-}(\alpha)\tilde{L}^{-}(\alpha) + \sum_{i=1}^{\infty} \frac{\hat{k}_{11}^{+}(\beta_i^+)S_i \exp(-\mathrm{i}\beta_i^+ d)}{\tilde{L}^{+}(\beta_i^+)(\alpha - \beta_i^+)} = \frac{\hat{k}_{12}^{+}(\alpha)}{\tilde{L}^{+}} \frac{(\alpha - u_0)(\alpha - u_0^*)}{(\alpha - v_0)(\alpha - v_0^*)} \\ - \left\{ \frac{\hat{k}_{11}^{+}(\alpha)k_{12}(\alpha)}{k_{11}(\alpha)\tilde{L}^{+}(\alpha)}\exp(-\mathrm{i}\alpha d) - \sum_{i=1}^{\infty} \frac{\hat{k}_{11}^{+}(\beta_i^+)S_i \exp(-\mathrm{i}\beta_i^+ d)}{\tilde{L}^{+}(\beta_i^+)(\alpha - \beta_i^+)} \right\}.\end{aligned} \tag{3.5}$$

Here

$$\tilde{L}(\alpha) = \frac{k_{11}k_{22} - k_{12}k_{21}}{k_{11}(\omega + \alpha M_2)\gamma_2 \Delta(\alpha - v_0)(\alpha - v_0^*)}, \tag{3.6}$$

and has been factorized in the form $\tilde{L}(\alpha) = \tilde{L}^+(\alpha)\tilde{L}^-(\alpha)$, with $\tilde{L}^\pm(\alpha)$ analytic and non-zero and with algebraic behaviour at infinity in the upper and lower halves of the complex α-plane respectively. In (3.5), S_i is the residue of k_{12}/k_{11} at $\alpha = \beta_i^+$, where the β_i^+ for $i = 1, 2, \ldots$ are the zeros of k_{11} in the upper half-plane. Note how the left and right-hand sides of (3.5) are analytic and possess algebraic behaviour at infinity in the lower and upper half-planes respectively. Proceeding as in the previous paragraph, we now set both sides of (3.5) to be unity again, thereby yielding two more equations, one containing the unknown functions $\hat{k}_{11}^+(\alpha)$ and $\hat{k}_{12}^+(\alpha)$ (see equation (B 2)) and the second containing the unknown function $\hat{k}_{12}^-(\alpha)$ (see equation (B 6)), both again in terms of the $\hat{k}_{11}^+(\beta_i^+)$.

Another four expressions identical to those described in the previous two paragraphs can be found by looking at the 2,1 and 2,2 elements in (2.24). Exactly the same procedure is followed, except that this time we take the entire functions to be $1, -1$ respectively (this will ensure that we obtain a linearly independent solution in the matrix equations which follow). All the factors $\hat{k}_{ij}^\pm(\alpha)$ are given in implicit form in Appendix B. To derive explicit expressions we set $\alpha = \beta_j^+$ in equation (B 1) and $\alpha = \beta_j^-$ in equation (B 6), leaving us with an infinite set of linear equations relating $\hat{k}_{12}^-(\beta_i^-)$ and $\hat{k}_{11}^+(\beta_i^+)$. These can be written in the matrix form

$$\sum_{j=1}^{\infty}(\mathscr{Y} - \mathscr{M}\mathscr{X}^{-1}\mathscr{M}^T)_{ij}A_j = 1 + \sum_{j=1}^{\infty}(\mathscr{M}\mathscr{X}^{-1})_{ij}, \qquad i = 1, 2, \ldots, \tag{3.7}$$

with

$$B_i = \mathscr{X}_{ii}^{-1} + \sum_{j=1}^{\infty}(\mathscr{X}^{-1}\mathscr{M}^T)_{ij}A_j. \tag{3.8}$$

Here

$$\left.\begin{aligned} A_i &= \frac{\hat{k}_{12}^-(\beta_i^-)\exp(\mathrm{i}\beta_i^- d)R_i}{L^-(\beta_i^-)} \quad B_i = \frac{\hat{k}_{11}^+(\beta_i^+)\exp(-\mathrm{i}\beta_i^+ d)S_i}{\tilde{L}^+(\beta_i^+)}, \\ \mathscr{X} &= \mathrm{diag}\frac{L^+(\beta_j^+)\tilde{L}^+(\beta_j^+)\exp(\mathrm{i}\beta_j^+ d)}{S_j} \quad \mathscr{Y} = \mathrm{diag}\frac{L^-(\beta_j^-)\tilde{L}^-(\beta_j^-)\exp(-\mathrm{i}\beta_j^- d)}{R_j}, \end{aligned}\right\} \tag{3.9}$$

and $\mathscr{M}_{ij} = 1/(\beta_j^+ - \beta_i^-)$. Note that the $\mathscr{M}_{ij}$ are always finite, because the modes β_j^+ and β_i^- lie in separate half-planes and do not coincide in our problem. The system (3.7) is truncated to finite dimension and solved using standard routines. (It proves convenient to work with the first iterate of the system by writing $\boldsymbol{A} = \overline{\boldsymbol{A}} + \mathscr{Y}^{-1}\boldsymbol{i}$, where $\boldsymbol{i}$ is the vector with unit elements, and then solving for $\overline{\boldsymbol{A}}$.) The unknown quantities $\hat{k}_{12}^-(\beta_i^-)$ and $\hat{k}_{11}^+(\beta_i^+)$ are thereby determined, and can then be substituted directly into (B 1), (B 6), (B 5), (B 2), so as to yield explicit expressions for four out of the eight elements in $\hat{k}_{ij}^\pm$. The remaining four elements can be obtained by first setting $\alpha = \beta_j^+$ in (B 3) and $\alpha = \beta_j^-$ in (B 8). We then have a matrix equation of a form almost identical to (3.7), except now with the 1 on the right-hand side replaced by -1 (this is why we chose the two arbitrary constants to be ± 1, so as to obtain different solutions to the two matrix problems). Solving then gives $\hat{k}_{21}^+(\beta_i^+)$, $\hat{k}_{22}^-(\beta_i^-)$, which are substituted into (B 3), (B 8), (B 7), (B 4). The factorization (2.24) for $d < 0$ is thereby complete.

4. Factorization of $\hat{\mathscr{K}}$ for a protruding nozzle

We now turn to the protruding configuration $d > 0$ shown in figure 1. As we will see, the method set out in the previous section for $d < 0$ needs to be modified in order for us to be able consider this new case.

We first equate the 1,2 elements in (2.24) to give

$$\hat{k}_{12}^{+}M^{+}(\alpha) = \frac{\hat{k}_{12}^{-}}{M^{-}(\alpha)} + \frac{\hat{k}_{11}^{-}k_{12}}{k_{22}M^{-}(\alpha)}\exp(-\mathrm{i}\alpha d), \tag{4.1}$$

where the scalar kernel $M(\alpha)$, given by

$$M(\alpha) = (\omega + \alpha M_2)\gamma_2\Delta(\alpha - u_0)(\alpha - u_0^*)/k_{22}, \tag{4.2}$$

has been factorized in the form $M(\alpha) = M^{+}(\alpha)M^{-}(\alpha)$, with $M^{\pm}(\alpha)$ analytic and non-zero and with algebraic behaviour at infinity in the upper and lower halves of the complex α-plane respectively.

We now compare (4.1) here with the corresponding equation (3.2) for the buried case $d < 0$. One key difference between (4.1) and (3.2) is the presence of the factor $\exp(-\mathrm{i}\alpha d)$ in the former as compared to $\exp(\mathrm{i}\alpha d)$ in the latter. Both these exponentials decay in the lower half-plane for $d > 0$ and $d < 0$ respectively, allowing us to determine Wiener–Hopf factors from (4.1) and (3.2) which behave algebraically at infinity. A second key difference between (4.1) and (3.2) is that in (3.2) the term k_{11} in the denominator of the second term on the right is a meromorphic function of α, allowing direct application of the pole removal method. However, in (4.1) the second term on the right contains the term k_{22} instead, and it can be shown from (2.22) that k_{22} is not meromorphic (in fact it has a logarithmic branch points at the zeros of γ_3 thanks to the ratio $\mathrm{K}_m(\gamma_3)/(\gamma_3\mathrm{K}'_m(\gamma_3))$). The pole removal method cannot therefore be used directly for $d > 0$, since not all the singularities of the second term on the right of (4.1) are poles. However, progress can be made using the procedure first suggested by Abrahams, in which a function which is not meromorphic is approximated to high accuracy by a Padé approximant. The latter, being a quotient of polynomials in α, is necessarily meromorphic; see Abrahams (2000) for a description of the use of Padé methods for scalar Wiener–Hopf problems, and Abrahams (2002) and Owen & Abrahams (2006) for their application in matrix problems.

In order to proceed we first need to approximate the non-meromorphic term

$$\mathrm{K}_m(\gamma_3)/(\gamma_3\mathrm{K}'_m(\gamma_3)).$$

Abrahams advocates the use of the two-point Padé approximant (see Baker & Graves-Morris 1996, p. 335ff for full details), in which the Padé coefficients are determined using two points in the complex α-plane, specifically in this case the origin and the point at infinity. In order to fix the behaviour at infinity it has been found more effective to consider first the function

$$F(\alpha) \equiv \frac{\mathrm{K}_m(\gamma_3)\mathrm{I}'_m(\gamma_3)}{\mathrm{K}'_m(\gamma_3)\mathrm{I}_m(\gamma_3)} + 1, \tag{4.3}$$

rather than working with $\mathrm{K}_m(\gamma_3)/(\gamma_3\mathrm{K}'_m(\gamma_3))$ directly. This is because if we approximate $F(\alpha)$ by an $[N-2, N]$† Padé approximant, then the leading-order behaviour at infinity of the ratio $\mathrm{K}_m(\gamma_3)/\mathrm{K}'_m(\gamma_3)$ will be captured exactly within the

† That is, the numerator and denominator are polynomials of degree $N-2$ and N respectively, for integer N.

Padé approximant of $F(\alpha)$. This certainly gives better behaviour for large $|\alpha|$ than would have been the case had we simply found a one-point Padé approximant of $\mathrm{K}_m(\gamma_3)/(\gamma_3\mathrm{K}'_m(\gamma_3))$ directly.

To proceed with the approximation we first expand the function $F(\alpha)$ as a power series in $\gamma_3(\alpha)$ about the point $\gamma_3(0)$ up to and including $O(\gamma_3^N)$. We then note that $\gamma_3(\alpha)$ is an even function of the Doppler-shifted complex variable $\alpha' = \alpha - (M_3\omega/\beta_3^2)$, and so expanding γ_3 as a power series in α' about $\alpha' = 0$ and substituting into our power series expansion of $F(\alpha)$, yields a new power series for $F(\alpha)$ containing only even powers of α' up to and including the $O(\alpha'^{2N})$ term. We now use this power series to uniquely form the $[N-2, N]$ Padé approximant of $F(\alpha)$ as the ratio of polynomials $P_{N-2}(\alpha')/Q_N(\alpha')$, so that finally we have that

$$\frac{\mathrm{K}_m(\gamma_3)}{(\gamma_3\mathrm{K}'_m(\gamma_3))} \approx \frac{\mathrm{I}_m(\gamma_3)}{(\gamma_3\mathrm{I}'_m(\gamma_3))}\left(\frac{Q_N - P_{N-2}}{Q_N}\right). \tag{4.4}$$

The right-hand side of (4.4) is now a meromorphic function of α.

The various power series and Padé approximants were calculated using built-in 'Series' and 'Pade' functions of MATHEMATICA©. In practice, we determined the power series expansions of each of the modified Bessel functions in (4.3) separately to high accuracy (typically each term to 64 decimal places), before recombining these series and substituting in the expansion of γ_3. This approach allowed us to increase the maximum number of terms calculated, and hence the value of N, within the limits of available computer memory. The maximum value of N we were then able to calculate (on a modern desktop PC) was typically $N = 40$, although smaller values of N could well be more than adequate for our purposes. An example calculation, with $N = 40$, is shown in figure 3. As can be seen, the exact and approximate expressions for k_{22} are visually indistinguishable along the inversion contour C, and the maximum relative error is at most 1.5%.

In our expression for k_{22}, equation (2.22), we now replace the term on the left of (4.4) by the meromorphic approximation given on the right of (4.4), leading to the approximation $k_{22} \approx k_{22}^p$. With this replacement the right-hand side of (4.1) is now a meromorphic function, and the pole removal method can now be applied exactly as in the previous section. Specifically, we now rearrange (4.1) to give

$$\begin{aligned}\hat{k}_{12}^+(\alpha)M^+(\alpha) - \sum_{i=1}^{\infty}\frac{\hat{k}_{11}^-(\delta_i^-)R_i\exp(-\mathrm{i}\delta_i^- d)}{M^-(\delta_i^-)(\alpha-\delta_i^-)} \\ = \frac{\hat{k}_{12}^-(\alpha)}{M^-(\alpha)} + \left\{\frac{\hat{k}_{11}^-(\alpha)k_{12}(\alpha)}{k_{22}^p(\alpha)M^-(\alpha)}\exp(-\mathrm{i}\alpha d) - \sum_{i=1}^{\infty}\frac{\hat{k}_{11}^-(\delta_i^-)R_i\exp(-\mathrm{i}\delta_i^- d)}{M^-(\delta_i^-)(\alpha-\delta_i^-)}\right\},\end{aligned} \tag{4.5}$$

where $\alpha = \delta_i^-$ for $i = 1, 2, \ldots$ are the zeros of k_{22}^p in the lower half-plane, and R_i is now the residue of k_{12}/k_{22}^p at $\alpha = \delta_i^-$. Equation (4.5) is exactly analogous to (3.4), and we proceed exactly as before by defining an entire function by the left/right of (4.5) in the upper/lower half-planes, and then taking this entire function to be unity. This then leads to an expression for the unknown function $\hat{k}_{12}^+(\alpha)$, and a relationship between the unknown functions $\hat{k}_{12}^-(\alpha)$ and $\hat{k}_{11}^-(\alpha)$, both in terms of the unknown values $\hat{k}_{11}^-(\delta_i^-)$, $i = 1, 2, \ldots$ (see equations (C 2) and (C 6)) in Appendix C.

We now equate the 1,1 elements in (2.24), which we use to eliminate $\hat{k}_{12}^-(\alpha)$ in the expression obtained by equating the 1,2 elements. Replacing k_{22} by the Padé approximant, and then removing the poles of the resultingmeromorphic functions,

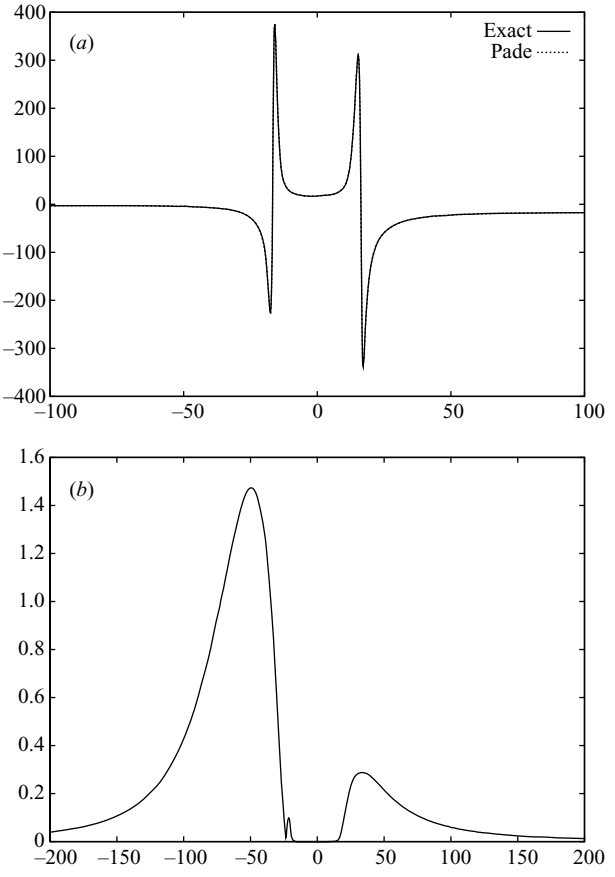

FIGURE 3. Comparison between the exact value of k_{22} and the Padé approximation k_{22}^p along the contour C (with Re(α) plotted along the horizontal). (*a*) Re$|k_{22}/\exp((1-a)\gamma_2(\alpha)|$ (the exponential factor is included to scale out the exponential growth of k_{22} at infinity for ease of comparison), and note that the exact and Padé curves are indistinguishable. (*b*) The percentage relative error, $100\times|1-k_{22}^p/k_{22}|$. Here $\omega=15$, $m=10$, $a=0.75$, $M_1=0.7$, $M_2=0.3$ and $M_3=0$.

yields

$$\hat{k}_{11}^-(\alpha)\tilde{M}^-(\alpha)-\sum_{i=1}^{\infty}\frac{\hat{k}_{12}^+(\delta_i^+)S_i\exp(\mathrm{i}\delta_i^+ d)}{\tilde{M}^+(\delta_i^+)(\alpha-\delta_i^+)}=-\frac{\hat{k}_{11}^+(\alpha)}{\tilde{M}^+(\alpha)}\frac{(\alpha-v_0)(\alpha-v_0^*)}{(\alpha-u_0)(\alpha-u_0^*)}$$
$$+\left\{\frac{\hat{k}_{12}^+(\alpha)k_{21}(\alpha)}{k_{22}^p(\alpha)\tilde{M}^+(\alpha)}\exp(\mathrm{i}\alpha d)-\sum_{i=1}^{\infty}\frac{\hat{k}_{12}^+(\delta_i^+)S_i\exp(\mathrm{i}\delta_i^+ d)}{\tilde{M}^+(\delta_i^+)(\alpha-\delta_i^+)}\right\}. \quad (4.6)$$

Here

$$\tilde{M}(\alpha)=\frac{k_{12}k_{21}-k_{11}k_{22}}{k_{22}(\omega+\alpha M_2)\gamma_2\Delta(\alpha-u_0)(\alpha-u_0^*)}, \quad (4.7)$$

and S_i is the residue of k_{21}/k_{22}^p at δ_i^+, where the δ_i^+ for $i=1,2,\ldots$ are the zeros of k_{22}^p in the upper half-plane. Exactly as before, the left/right-hand sides of equation (4.6) define a function which is analytic in the lower/upper half-planes, which by analytic continuation defines an entire function which we again set to unity. This yields equations involving $\hat{k}_{11}^-(\alpha)$ and $\hat{k}_{11}^+(\alpha)$ and $\hat{k}_{12}^+(\alpha)$, both in terms of the unknown $\hat{k}_{12}^+(\delta_i^+)$ (see equations (C 5) and (C 1)).

So far we have found four equations for the unknown factors, and the remaining four equations can be found by looking at the 2,2 and 2,1 elements in (2.24). Since this is done in exactly the same way as described in the previous section, with suitable modification to account for the use of the Padé approximant, we need not supply details here but simply collect all eight elements of the matrix factorization together in Appendix C. These elements are still given in terms of the unknowns sets of coefficients $\hat{k}^{-}_{11,21}(\delta_i^-)$ and $\hat{k}^{-}_{12,22}(\delta_i^+)$, and the algebraic equation which needs to be solved in order to obtain these unknowns, exactly analogous to (3.7), is also given in Appendix C.

Finally, we note here that when using Padé approximants it is important to take care when evaluating the approximate matrix factors outside their range of analyticity. For instance, if one wished to evaluate $\hat{\mathscr{K}}^{+}$ in the lower half-plane, then one should evaluate $\hat{\mathscr{K}}^{-}\hat{\mathscr{K}}$, since the Padé approximation for $\hat{\mathscr{K}}^{-}$ is valid in the lower half-plane.

5. An approximation to the sound field for a buried nozzle

The solution presented already for the buried case $d<0$ is exact, but a simplified approximate solution can be derived which sheds light on the scattering processes. An approximate solution for the buried nozzle configuration has been given by Taylor *et al.* (1993), in the low-frequency limit in which the only acoustic modes which propagate inside the duct are the axisymmetric (i.e. $m=0$) plane-wave modes. Their analysis can easily be extended to the more general case in which a spinning mode propagates inside the duct, and that is what we will present here.

Taylor *et al.*'s idea is to first consider the scattering of the incident field by the cylinder edge $r=a, x=d$ in isolation, to yield a finite family of cut-on modes and a Kelvin–Helmholtz mode associated with the vortex sheet $r=a$, all propagating downstream in $d<x<0$. These modes are then rescattered by the cylinder edge $r=1, x=0$, and so radiate to the far field. In this approximation, the multiple scattering and rescattering by the two edges is ignored, as is the interaction between the acoustic and hydrodynamic near fields of each edge with the other edge. The approximation will therefore not be valid when d is comparable to, or smaller than, a typical axial wavelength, and even then will not be valid in cases where there are significant reflections of downstream-going modes by the open end $x=0$, as would happen for instance in resonant or near-resonant situations. However, the big advantage of treating the edge scattering problems separately is that one now simply solves two scalar Wiener–Hopf problems, which can be done in a standard way. This is exactly what was undertaken by Taylor *et al.* at low frequency, and we therefore do not need to reproduce the full details of our calculation here. For simplicity, we present results only for the case of the incident mode present in $a\leqslant r\leqslant 1$; incident modes in $r\leqslant a$ can easily be included but only complicates the results.

In the first scalar Wiener–Hopf problem we take the cylinder $r=1$ to be doubly infinite, and then calculate the scattering of the incident field ϕ^b_{inc} by the semi-infinite cylinder $r=a, x'<0$ and the vortex sheet $r=a, x'>0$ where $x'=x-d$. After some algebra, we find the scalar Wiener–Hopf equation for this problem in the form

$$\begin{aligned}\frac{\Phi_r^+(\alpha,a+)(\alpha-v_0)(\alpha-v_0^*)}{L^+(\alpha)} &- \frac{L^-\big(\alpha^{b,-}_{inc}\big)g}{\big(\alpha-\alpha^{b,-}_{inc}\big)}\\ &= \frac{g\big[L^-(\alpha)-L^-\big(\alpha^{b,-}_{inc}\big)\big]}{\alpha-\alpha^{b,-}_{inc}} + D_1(\omega+\alpha M_1)\Phi^-(\alpha,a-)L^-(\alpha)\\ &- D_2(\omega+\alpha M_2)\Phi^-(\alpha,a+)L^-(\alpha) + L^-(\alpha)\{\mathrm{i}M_1\phi(0,a-)-\mathrm{i}M_2D_2\phi(0,a+)\}. \quad (5.1)\end{aligned}$$

The notation used in this equation is exactly as used already. We can now proceed simply by noting that the left/right-hand sides of this equation define functions which are analytic in the upper/lower halves of the α-plane, to yield an entire function by analytic continuation. Moreover, using the same arguments as already deployed in § 2.4 about the behaviour at infinity, it follows that this entire function is identically zero, so that now the unknown normal velocity $\Phi_r^+(\alpha, a+)$ is given from (5.1) and the scattered field can be found. In particular, we find that the downstream-going scattered potential in $d < x < 0$, $a < r < 1$ is

$$\phi = \sum_i A_i [-\mathrm{K}_m'(\gamma_2(\beta_i^-))\mathrm{I}_m(\gamma_2(\beta_i^-)r) + \mathrm{I}_m'(\gamma_2(\beta_i^-))\mathrm{K}_m(\gamma_2(\beta_i^-)r)] \exp(-\mathrm{i}\beta_i^- x'), \quad (5.2)$$

where

$$A_i = \frac{\mathrm{i}L^-(\alpha_{inc}^{b,-})(\omega + M_2\beta_i^-)r_i g}{L^-(\beta_i^-)(\beta_i^- - \alpha_{inc}^{b,-})}. \quad (5.3)$$

Here r_i is the residue of $1/k_{11}$ at $\alpha = \beta_i^-$ and the summation in (5.2) is over the Kelvin–Helmholtz mode and the downstream cut-on modes of k_{11}. Equation (5.3) describes the field only in $a \leqslant r \leqslant 1$; a similar expression for the scattered field in $r \leqslant a$ can also be derived but is not required for our present purposes.

In the second scalar Wiener–Hopf problem the cylinder $r = a$ is now ignored, and the downstream-going waves described by (5.2) are treated as being an incident field propagating inside the semi-infinite cylinder $r = 1$, $x < 0$ with a doubly infinite vortex sheet on $r = a$. The scalar Wiener–Hopf equation now turns out to be

$$\begin{aligned}\tilde{L}^+(\alpha)(\alpha - v_0)(\alpha - v_0^*)\Phi_r^+(\alpha, 1-) - \mathrm{i}D_2 \sum_i \frac{A_i \exp(\mathrm{i}\beta_i^- d)(\omega + M_2\beta_i^-)}{\gamma_2(\beta_i^-)(\alpha - \beta_i^-)\tilde{L}^-(\beta_i^-)} \\ = \frac{(\omega + \alpha M_3)\Phi^-(\alpha, 1+) + \mathrm{i}M_3\phi(0, 1+) - D_2(\omega + \alpha M_2)\Phi^-(\alpha, 1-) - \mathrm{i}M_2 D_2\phi(0, 1-)}{\tilde{L}^-(\alpha)} \\ + \mathrm{i}D_2 \sum_i \frac{A_i \exp(\mathrm{i}\beta_i^- d)(\omega + M_2\beta_i^-)}{\gamma_2(\beta_i^-)(\alpha - \beta_i^-)} \left[\frac{1}{\tilde{L}^-(\alpha)} - \frac{1}{\tilde{L}^-(\beta_i^-)}\right]. \quad (5.4)\end{aligned}$$

Again, the left/right-hand sides are analytic in the upper/lower halves of the α-plane, and we can argue as before that they describe by analytic continuation an entire function which is identically zero. The second scattered field is thereby found, and in particular, we find the quantity $\Phi_r^+(\alpha, 1^-)$ in the form

$$\frac{\mathrm{i}D_2}{\tilde{L}^+(\alpha)(\alpha - v_0)(\alpha - v_0^*)} \sum_i \frac{A_i \exp(\mathrm{i}\beta_i^- d)(\omega + M_2\beta_i^-)}{\gamma_2(\beta_i^-)\tilde{L}^-(\beta_i^-)(\alpha - \beta_i^-)}, \quad (5.5)$$

which is to be compared with the more complicated exact result given through (2.28). The acoustic far field can now be found by applying the method of steepest descents exactly as was done for the full problem, so that the approximate acoustic pressure is again given in (2.32), but now with $\Phi_r^+(\alpha, 1^-)$ given explicitly in (5.5). Note that this second scalar scattering problem has recently been studied in much greater depth by Samanta & Freund (2008).

In summary, in this simplified model we can see the way in which the single incident mode is scattered into a series of modes in $d \leqslant x \leqslant 0$ by the first edge, and these modes are in turn scattered into far-field sound at the second edge.

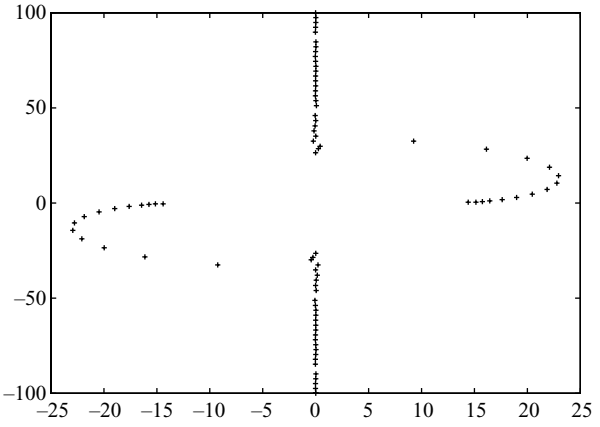

FIGURE 4. The locations of the zeros of the [40 : 40] Padé approximation to k_{22} in the complex α-plane. Here $\omega = 15$, $m = 4$, $a = 0.75$ and the mean flow is zero everywhere.

6. Results

In this section we will present a range of results, first for zero mean flow and then for non-zero mean flow. We will be concerned with the far-field directivity function $D(\Theta)$, which is given in terms of the matrix Wiener–Hopf solution described in the previous sections. We will for the most part suppose that the incident field has total power input of unity, and in what follows we will plot the quantity $20\log_{10}|D(\Theta)|$ as the normalized sound pressure level. Throughout we present results for the cold jet case $C_j = D_j = 1$.

6.1. *No mean flow*

In this subsection we take all $M_j = 0$, but retain the key geometrical ingredient of non-zero d. With relevance to the protruding case $d > 0$ we plot in figure 4 the zeros of the Padé approximation k_{22}^p. For zero flow it turns out that the exact k_{22} has no zeros, but has logarithmic branch points at $\alpha = \pm\omega\,(= \pm 15)$, and interestingly the Padé approximation, while having no branch cuts, has zeros which lie along lines joining $\pm\omega$ to infinity through the upper and lower half-planes, thereby mimicking the branch cuts. It is important to identify all the relevant zeros of k_{22}^p, because for small d the series in equations (C 1)–(C 8) are only slowly convergent and one must not miss out any Padé zeros which are close to the real axis. This was checked by using winding-number calculations (Brazier-Smith & Scott 1991) to identify the number of zeros contained within finite regions of the α-plane, before using Newton iteration to locate the zeros accurately.

We have validated the zero-flow results in two ways. First, we have computed the total power radiated as the sum of the power radiated to the far field plus the power reflected back into the bypass duct and jet pipe (the latter two being given using the equations presented in § 2.6), and verified that this equals the (unit) input power to numerical accuracy. Second, we have found excellent agreement between our analytical results and numerical results from the finite-element code Actran (©Free Field Technologies) computed by Mr Parcelier and Dr Sugimoto of ISVR, University of Southampton (private communication 2007).

In figure 5 we plot the far-field directivity in the unstaggered case $d = 0$ for a single incident mode in the bypass duct. For these parameters there are two downstream cut-on radial modes in the bypass, and we consider the (well cut-on) first radial mode.

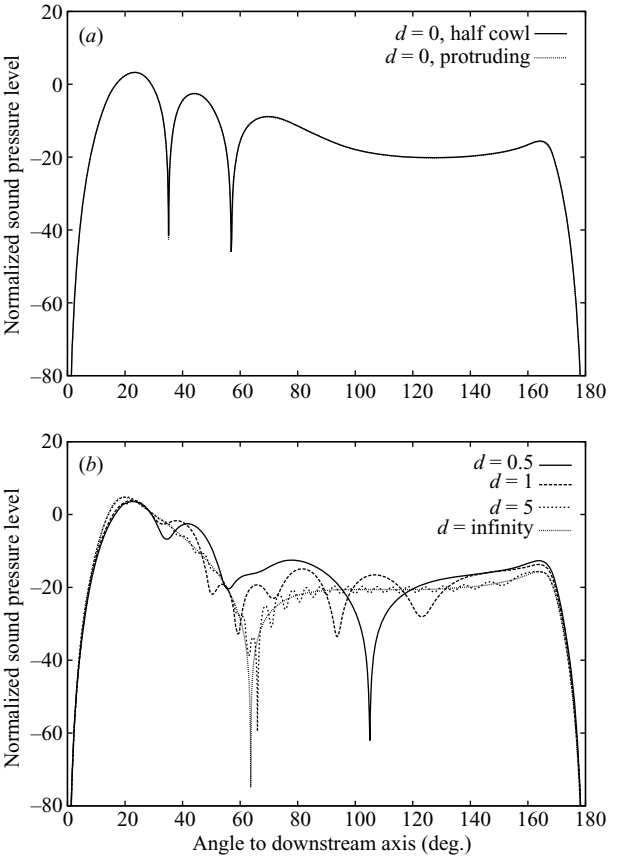

FIGURE 5. The far-field acoustic pressure for various values of d, with $\omega = 15$, $m = 4$, $a = 0.75$ and the mean flow is zero everywhere. The incident field is the first cut-on mode in the bypass duct. In (a) the case $d = 0$ is calculated using both the $d < 0$ and the $d > 0$ methods, and the two curves are visually indistinguishable.

The directivity here has been obtained in two ways: by taking the $d \to 0-$ limit of the buried nozzle solution and by taking the $d \to 0+$ limit of the protruding solution. Of course, these two solutions are derived in different ways, so it is an excellent check of our results that the curves in figure 5 are visually indistinguishable (in fact, there is a minute difference between the two cases, fully consistent with the fact that the Padé solution involves a very small error, as seen in the previous section).

In figure 5 we see the effect of changing the value of d in the protruding configuration. Notice that the position and amplitude of the peak radiation direction, here at about 20°, is rather insensitive to the value of d. This can easily be understood by considering the incident mode. At high frequency Chapman (1994) has shown that a duct mode can be represented as a family of rays following piecewise-linear helices. These helices make an angle θ_{mn} with the cylinder axis when projected onto a plane of constant θ, where m and n refer to the mode azimuthal and radial order respectively. It follows that the incident axial wavenumber is $\alpha_{inc}^{b,-} = -\omega \cos\theta_{mn}$. Further, Keith & Peake (2002) have shown that the peak radiation direction in the far field is close to $\Theta = \theta_{mn}$, which is due to the fact that the peak radiation corresponds to the transition region in the primary diffracted field of the incident mode scattered by the outer

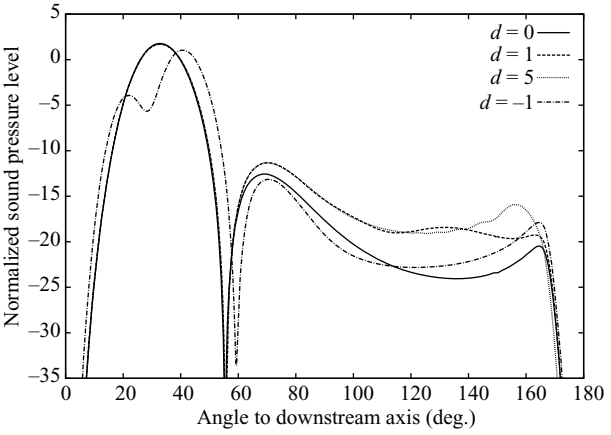

FIGURE 6. The far-field acoustic pressure for various values of d, with $\omega = 15$, $m = 4$, $a = 0.75$ and the mean flow is zero everywhere. Here the incident mode is the first cut-on mode in the core.

cylinder edge. The incident mode is of course unaffected by the value of d, explaining the insensitivity of the results in figure 5 around $\Theta \approx 20^\circ$ (note that the frequency used here is not very high, which perhaps explains the small discrepancy between the location of the peak direction and the value $\theta_{mn} = 17.8^\circ$ for the parameter values used in figure 5).

Away from the peak radiation direction in figure 5, and in particular in directions which are close to the perpendicular to the axis, the field shape is much more sensitive to the value of d. This is hardly surprising, since observers in these areas receive both the direct scattered field from the outer lip and the rescattering of that direct field by the inner lip. Changing the relative phasing of these two sources by changing their separation will lead to changes in the field shape. As the value of d gets larger, however, the effect of the rescattering by the inner lip must reduce (since the direct field from the outer edge decays with distance and is correspondingly weaker by the time it reaches the inner edge). This can be seen in figure 5, where the field shape for $d = 5$ is close to the result labelled $d = \infty$ of Gabard & Astley (2006), who considered an infinite centrebody. Notice, however, that for the relatively large but finite value of $d = 5$ the general shape of the directivity oscillates about the $d = \infty$ result, which can still be attributed to the interference between the diffracted field from the outer and inner lips (the latter of course being absent in the Gabard & Astley solution). In the standard problem of interference between two identical sources located a distance D apart, one expects constructive/destructive interference in the far field, with the angular separation between adjacent interference fringes being $O(\omega D)$. Of course, the sources corresponding to the scattering by the two edges are not identical, and this is why we see only small oscillations for $d = 5$ about the $d = \infty$ result in figure 5. However, the angular length scale of the oscillations is consistent with this interference interpretation, and as $d \to \infty$ both the angular separation and the amplitude of the oscillations decrease to zero.

In figure 6 we consider an incident core mode. As might be expected on simple geometrical grounds, the field shapes for the values $d = 1, 5$ are almost identical for most observer positions, and indeed are almost identical to the radiation pattern for sound emission from a single cylinder. The $d = 1, 5$ field shapes do differ from each other, but only over a small portion of observer angle in the far rearward arc,

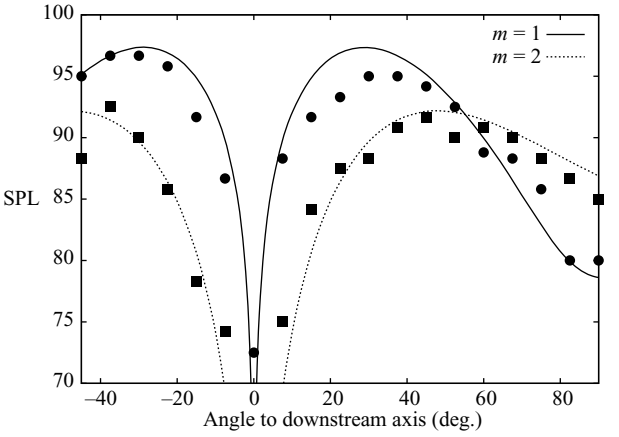

FIGURE 7. Far-field sound pressure levels for an unstaggered nozzle with no mean flow; comparison of experiments of Plumblee & Dean (1973*a*, *b*) (circles $m = 1$, squares $m = 2$) with present theory (lines).

which can be attributed to the blocking effect of the outer lip on the field from the inner lip. Both $d = 1, 5$ results are very close to the $d = 0$ result in the forward arc, which is also to be expected since in the forward arc the field is dominated by noise radiated directly from the jet pipe. The position of the main lobe, as noted earlier, is determined by the incident mode in the core, which in this case has $\theta_{mn} = 28.21°$. Of course, in the rearward arc the shielding effect of the outer cylinder explains why the $d = 0$ result is significantly lower than the $d = 1, 5$ levels. In the buried nozzle case $d = -1$, notice that there are now two lobes in the forward arc. This can be understood by noting that in this case the single incident core mode is scattered into three downstream-going cut-on modes in $d \leqslant x \leqslant 0$, and that two of these modes (with $\theta_{mn} = 20.8°$ and $\theta_{mn} = 38.2°$) are now radiating strongly to the far field. We will return to the issue of the contributions from the various modes in $d \leqslant x \leqslant 0$ when we consider non-zero flow.

Finally in this subsection we attempt to compare some of our predictions with the experimental results of Plumblee & Dean (1973*b*), who considered the radiation properties of a coaxial duct with $d = 0$. We consider the zero-flow case presented in figures 4 and 5 of Plumblee & Dean (1973*a*), for which $a = 0.566$, $\omega = 4.485$ and $m = 1, 2$ respectively. Plumblee & Dean report both the far-field pressure pattern and the pressure around the inner rim of the outer cylinder (i.e. on $x = 0, r = 1-$ in our notation). However, it is the amplitude of the incident mode in the duct which is required as the fundamental input into our theoretical prediction, and this value is not reported for the experiment. To make an absolute-level comparison we therefore use equation (2.34) to calculate the pressure on the rim $x = 0, r = 1-$ in the form of a standing wave whose amplitude is directly proportional to the incident-mode amplitude. We then choose the incident-mode amplitude (a single number) to achieve the experimentally measured rim pressure. The predicted far-field pressure is then completely determined using (2.32), and the results are shown in figure 7. The agreement is quite satisfactory over the measured angular range $-45° \leqslant \Theta \leqslant 90°$, with the general field shape and relative levels captured quite well. Note, however, that in the experiments the nominally single-mode incident field was polluted with other incident azimuthal orders, leading to oscillations in the field shape and asymmetry

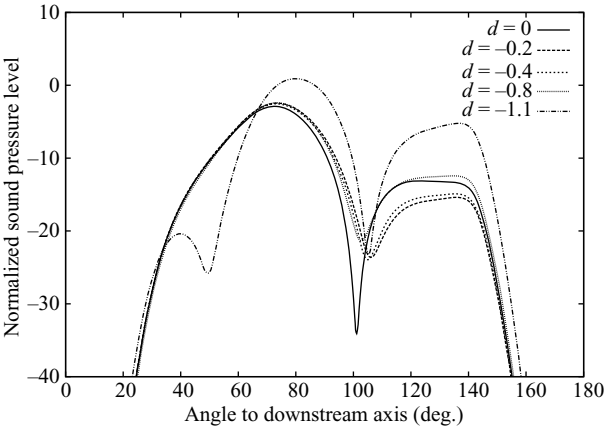

FIGURE 8. Comparison of normalized far-field sound pressure levels for various buried nozzles. Here $M_1 = 0.7$, $M_2 = 0.3$, $M_3 = 0$, $\omega = 15$, $m = 10$, $a = 0.75$ and the incident mode is the single cut-on downstream mode in the bypass.

about $\Theta = 0$ of amplitude of order 2 dB, which could certainly account for what discrepancies are seen in figure 7.

6.2. *Effects of mean flow*

We now turn our attention to the case of non-zero mean flow. One effect of the presence of the mean shear between the jet, bypass and exterior flows is to refract the scattered sound so as to shift the location of the lobes in the far field, see for instance Plumblee & Dean (1973*b*). However, we shall concentrate here on a different effect, which is particular to the staggered nozzle geometry we are studying, and that is the way in which the Kelvin–Helmholtz instability wave shed from the inner lip in the buried case (or the outer lip in the protruding case) interacts with the outer lip (or the inner lip in the protruding case) downstream.

Some results for a series of negative d are shown in figure 8. Notice that the levels in the rearward arc are significantly lower for $d = -0.2, -0.4$ than for $d = 0$. This indicates that the rearward noise is in part due to scattering from the lip of the inner cylinder, which is being shielded as the inner cylinder becomes more deeply buried. However, as d becomes more negative the rearward noise level rises again, and once $d = -0.8$ we can see that it has returned to a similar level to the unstaggered case. This can be understood by noting that the field in $d < x < 0$ possesses a pole contribution from the Kelvin–Helmholtz instability mode $\alpha = v_0$ of the jet/bypass shear layer. If we ignore the presence of the outer cylinder, then it follows that the instability decays away from $r = a$ (and of course grows downstream), so that, at least close to the edge of the inner cylinder, the instability wave will grow like

$$|\exp(-\gamma_2(v_0)|r - a| - \mathrm{i}v_0 x)|. \tag{6.1}$$

As pointed out by Gabard & Astley (2006), it follows that the influence of the instability is felt within a downstream-pointing cone making an angle $\tan^{-1}[\mathrm{Im}(v_0)/\mathrm{Re}(\gamma_2(v_0))]$ with the axis. For the parameter values used in figure 8 this angle is 21.44°. For small values of d this cone will not intersect with the edge of the outer cylinder, but for d more negative than the critical value -0.637 the outer edge will lie inside the cone. Once this happens the instability mode can be significantly scattered into the acoustic field by the outer edge, and as we will see in a

moment this is why the levels for $d = -0.8$ in figure 8 have increased in the rearward arc. As the value of $-d$ increases yet further, the outer edge moves deeper into the instability-mode cone, and the amplitude of the instability wave as it reaches that edge is correspondingly greater (see the $d = -1.1$ levels in figure 8).

At this point we turn to the approximate solution for the buried case given in § 5, and results for the cases considered in figure 8 are shown in figure 9. The approximate method is based on the idea of the incident mode in $x < d$ (which for these parameters has mode number -6.470) being scattered by the inner cylinder edge into the instability mode ($\alpha = v_0$) of the shear layer $r = a$ and downstream cut-on acoustic modes in $d < x < 0$ (here there are two cut-on acoustic modes, with wavenumbers -5.79 and 3.47, denoted in figure 9 as mode 1 and mode 2 respectively). These three modes are then scattered by the edge of the outer cylinder to give the approximate far-field noise. In figure 9(*a*) we see that the exact and approximate solutions are in close agreement. This means that the effect which is absent from the approximate solution, namely the multiple rescattering of modes travelling up and down in $d \leqslant x \leqslant 0$, is of little importance in this case. The contribution to the far-field pressure by the scattering of the instability mode is negligible and has not been plotted. This corresponds to the case in which the outer edge lies outside the instability-mode cone of influence. Note also in this case that the incident wave is scattered more efficiently into the acoustic mode labelled '1', which is hardly surprising since this is the mode whose wavenumber is closer to that of the incident mode.

In figure 9(*b*) we have $d = -0.8$, in which case the outer edge lies just inside the instability-wave cone. The contribution from the instability mode is now more significant, while the contributions from the two acoustic modes are largely unchanged. The scattering of the instability mode has a noticeable effect on the total noise in the rearward arc, since this is where the noise from the scattering of the acoustic modes is lower. Finally, in figure 9(*c*) we have $d = -1.1$, the outer edge lies well inside the instability-wave cone, and the approximate solution is dominated by the scattering of the instability wave. The agreement between the approximate and exact solutions is now very poor, and this shows that the scattering of the large-amplitude instability wave into upstream-going acoustic modes, and their subsequent interaction with the edge of the inner cylinder, is an important effect. Even so, our hypothesis of the increased importance of the instability wave of the inner shear layer is confirmed.

Finally in this section we present in figure 10 results for the protruding case with flow. Just as with zero flow, notice how the field in the main-beam direction is largely unaffected as d increases from zero (see figure 5), while the field in the rearward arc undergoes appreciable modification. The instability wave of the shear layer emanating from the outer lip has wavenumber $u_0 = -50.86 + 49.76\mathrm{i}$ with $\gamma_2(u_0) = 51.96 - 48.64\mathrm{i}$, so that the cone of influence for this mode makes an angle 43.76° with the axis, and the critical value of d for which the edge of the inner cylinder lies exactly on this cone is $d = 0.26$. As we can see, the radiation increases significantly for $d = 0.35$, once the inner edge is well within the instability-wave cone. It therefore follows that the scattering of the instability wave can have an appreciable effect on the noise for both buried and protruding configurations.

7. Concluding remarks

We have presented the analytical solution for the noise radiation from a coaxial exhaust system carrying mean flow, in which the open end of the inner cylinder is either buried or protrudes by a finite distance. We believe this is a highly non-trivial

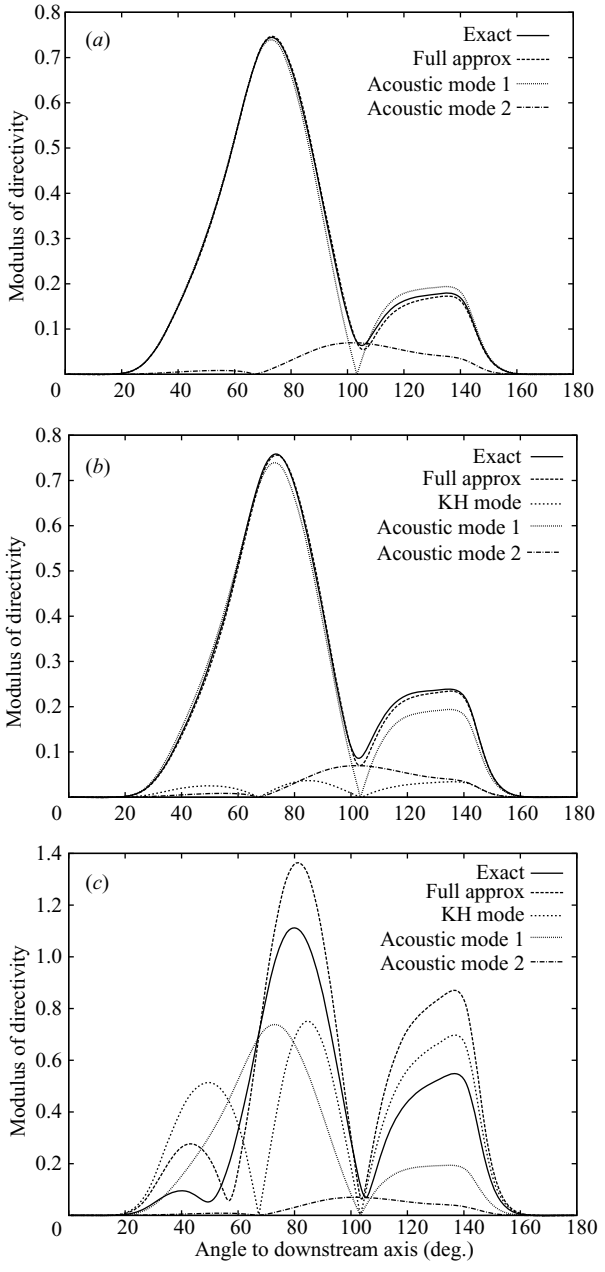

FIGURE 9. Far-field pressure directivity for a buried nozzle with mean flow; comparison between the exact solution and the approximate solution of § 5, together with the various components making up the approximate solution. On the vertical axis we plot $|D(\Theta)|$, with the incident field normalized to unit total power. $M_1 = 0.7$, $M_2 = 0.3$, $M_3 = 0$, $\omega = 15$, $m = 10$, $a = 0.75$ and the incident mode is the single cut-on downstream mode in the bypass. (*a*) $d = -0.4$, (*b*) $d = -0.8$ and (*c*) $d = -1.1$. In (*a*) the contribution of the Kelvin–Helmholtz (KH) instability mode is negligible and is not plotted.

extension of the important problem solved by Munt (1977), who considered a single cylinder with mean flow. This has required solution of a matrix Wiener–Hopf problem. For the buried case this has been solved directly using the well-known pole removal

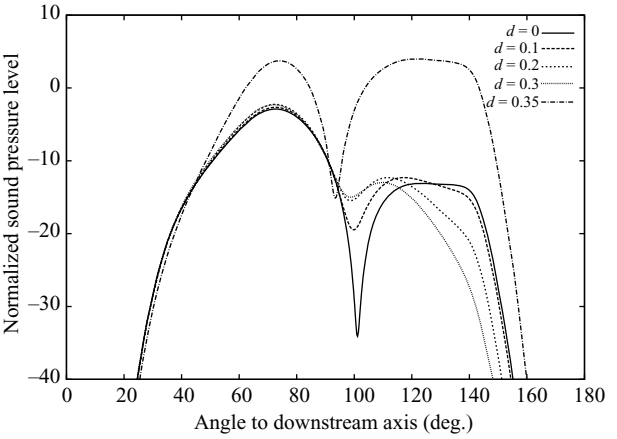

FIGURE 10. Far-field pressure directivity for a protruding nozzle with mean flow; comparison of normalized far-field sound pressure levels for various protruding nozzles. Here $M_1 = 0.7$, $M_2 = 0.3$, $M_3 = 0$, $\omega = 15$, $m = 10$, $a = 0.75$ and the incident mode is the single cut-on downstream mode in the bypass.

technique, but in the protruding case it has first required the application of Padé approximants, Abrahams (1997, 2000), to convert the problem into a form suitable for the application of the pole removal technique. From a physical point of view, the reason for the change in character of the solution is clear: one is attempting to match a waveguide field upstream with an acoustic far field through the intermediate region of length $|d|$ between the two open ends; in the buried case the field in this overlap region is composed of plane waves, and is therefore modal, while in the protruding case the field is allowed to propagate out towards infinity in the lateral directions. The use of the Padé approximant can be viewed as introducing an effective 'waveguide', in which 'novel' wall conditions in some sense mimic the genuine lateral unboundedness. We can also view our use of Padé approximants as being an alternative to the integral-equation method of Abrahams & Wickham (1990*a*) for factorizing Wiener–Hopf matrices containing exponential phase factors.

A key feature of our solution has been the inclusion of mean shear between the jet, bypass and exterior. The application of the full Kutta condition determines the amplitude of the Kelvin–Helmholtz waves launched from the trailing edges, and this has an effect on the noise levels (for instance, a different radiated sound field would be obtained in our problem if a so-called 'no Kutta condition' solution were adopted, as seen in the related half-lined centrebody problem of Demir & Rienstra (2006)). Once launched these instability waves do not influence the far-field sound within the confines of the linear theory used here, unless some other mechanism is present to rescatter them into the acoustic field. In the Munt and Gabard & Astley problems no such mechanism is present, but in our case the presence of two sharp edges means that the Kelvin–Helmholtz waves launched from the upstream edge can be scattered into acoustic waves by their interaction with the downstream edge. Because the instability waves grow in the axial direction but decay in the lateral direction, and are therefore of appreciable amplitude only within cones emanating from the edge from which they were shed, it follows that the rescattering will only occur if the two edges are sufficiently far apart for the second edge to lie within this cone. This effect has been clearly seen in our solution for both the buried and protruding configurations, with the noise increasing appreciably once the downstream edge starts to interact

with the upstream instability wave. The numerical values we have obtained for the resulting sound levels rely on our model of the shear layer as a vortex sheet, which of course tends to overestimate the spatial growth rates involved. Before definitive statements can be made about the likely significance of this effect for a real engine geometry, further investigation using more realistic shear-layer models are required. Other effects, such as the inclusion of acoustic lining and the transition from acoustic near- to far-field behaviour, are also under current consideration. A supersonic jet could also be modelled, in which the case the branch cuts for the function $\gamma_1(\alpha)$ would need to be changed so as to join both the branch points to infinity through the lower half-plane.

The majority of this work was completed while B. V. held a David Crighton Fellowship in DAMTP, January–June 2005. Mr B. Parcelier, Drs R. Sugimoto & G. Gabard and Professor J. Astley of ISVR, University of Southampton are gratefully acknowledged for the provision of Actran data for validation purposes, together with a number of helpful discussions. Advice from Professor I. D. Abrahams about the use of his Padé technique is also acknowledged. The authors note that Dr S. Rienstra has also been working on the buried-nozzle problem.

Appendix A. Scalar factorization of various kernels

As part of the factorization of the Wiener–Hopf matrix we have to complete the multiplicative factorization of the scalar functions $L(\alpha)$, $\tilde{L}(\alpha)$, $M(\alpha)$ and $\tilde{M}(\alpha)$. Consider first $L(\alpha)$ and write

$$L(\alpha) = \left[\frac{(\omega + \alpha M_2)\gamma_2}{D_2 M_2^2 + D_1 M_1^2(\beta_2/\beta_1)}\right]\left[\frac{(\alpha - v_0)(\alpha - v_0^*)}{(\alpha - w_0)(\alpha - w_0^*)}\right]\mathscr{L}(\alpha), \tag{A 1}$$

where

$$\mathscr{L}(\alpha) \equiv \left(D_2 M_2^2 + D_1 M_1^2 \frac{\beta_2}{\beta_1}\right)\frac{\Delta(\alpha - w_0)(\alpha - w_0^*)}{k_{11}}. \tag{A 2}$$

The function $\mathscr{L}(\alpha)$ has the important properties that it is non-singular at the Kelvin–Helmholtz wavenumber w_0 (and at w_0^*) of k_{11}, and that $\mathscr{L}(\alpha) \to 1$ as $\alpha \to \infty$ along the real axis. The multiplicative factorization $\mathscr{L}(\alpha) = \mathscr{L}^+(\alpha)\mathscr{L}^-(\alpha)$, with $\mathscr{L}^\pm(\alpha)$ analytic and non-zero in the upper/lower halves of the α-plane, can then be completed using the standard expressions

$$\mathscr{L}^\pm(\alpha) = \exp\left[\pm\frac{1}{2\pi\mathrm{i}}\int_C \frac{\log\mathscr{L}(\xi)}{\xi - \alpha}\mathrm{d}\xi\right]. \tag{A 3}$$

The contour C is the real axis deformed to lie above/below all poles and zeros of $\mathscr{L}$ lying in the lower/upper half-plane (but note that C need not be deformed above $\alpha = w_0$, since the k_{11} Kelvin–Helmholtz mode has been explicitly factored out of $\mathscr{L}$). We have used the parametric form for C proposed by Rienstra,

$$\alpha = t + \mathfrak{C} - \frac{4\mathrm{i}\mathfrak{D}(t/\mathfrak{W})}{3 + (t/\mathfrak{W})^4}, \tag{A 4}$$

where $-\infty < t < \infty$, and a typical example is shown in figure 2. The value of $\mathfrak{C}$ is the intercept with the real axis, and is chosen by looking at all the neutral modes of $k_{11,22}$, Δ and $\det\mathscr{K}$ and setting $\mathfrak{C}$ to lie halfway between the largest/smallest neutral

modes in the lower/upper half-planes. The width and height parameters $\mathfrak{W}$ and $\mathfrak{D}$ are chosen to ensure that C lies above/below all modes in the lower/upper half-planes.

Some care must be taken when evaluating the complex logarithm found in equation (A 3) and elsewhere. One approach, as adopted by Demir & Rienstra (2006), is to insert a logarithmic branch cut and then insist that the integration contour C must be chosen so as to avoid $\mathscr{L}(\xi)$ crossing this branch cut, so that $\log\mathscr{L}(\xi)\to 1$ at both ends of C. We have taken a different approach, however, which is to insist that the argument of $\log\mathscr{L}(\xi)$ varies continuously along the contour C (and therefore potentially varies outside the range $-\pi<\arg[\log\mathscr{L}(\xi)]<\pi$). It is certainly the case that $|\log\mathscr{L}(\xi)|\to 1$ at both ends of C in our method, but there is now the possibility that $\arg[\log\mathscr{L}(\xi)]\to\nu$ as $\xi\to-\infty$ and $\arg[\log\mathscr{L}(\xi)]\to\mu$ as $\xi\to\infty$, with μ,ν non-zero. If $\mu\neq\nu$ then the integral in (A 3) does not converge. However, this eventuality has been discussed by Noble (1988, p. 41, example 1.12); the idea is to use (A 3) to factorize instead the function

$$\mathscr{L}(\xi)\exp(-\mathrm{i}\mu)\frac{[\xi-\tau_-]^{(\mu-\nu)/2\pi}}{[\xi-\tau_+]^{(\mu-\nu)/2\pi}}, \tag{A 5}$$

where $\tau_\pm$ are suitably chosen complex constants in the upper and lower half-planes respectively. The additional factors introduced into (A 5) can then be easily factorized on sight to finally yield the factors of $\mathscr{L}(\alpha)$

The integral in (A 3) can be easily computed numerically by first splitting it into two semi-infinite integrals over $t\lessgtr 0$, sending t to $-t$ in the $t<0$ integral, and then mapping the resulting sum onto a finite interval $0\leqslant s<1$ using the transformation $t=s/(1-s)^2$ suggested by Rienstra. Standard quadrature routines can then be used to evaluate the finite integral.

Having completed the factorization of $\mathscr{L}(\alpha)$, the factorization of $L(\alpha)$ can now proceed in an elementary fashion, and from (A 1) we find

$$\left.\begin{aligned} L^-(\alpha) &= \frac{\gamma_2^-(\alpha)}{\left(D_2M_2^2+D_1M_1^2(\beta_2/\beta_1)\right)^{1/2}}\mathscr{L}^-(\alpha),\\ L^+(\alpha) &= \frac{(\omega+\alpha M_2)\gamma_2^+(\alpha)}{\left(D_2M_2^2+D_1M_1^2(\beta_2/\beta_1)\right)^{1/2}}\left[\frac{(\alpha-v_0)(\alpha-v_0^*)}{(\alpha-w_0)(\alpha-w_0^*)}\right]\mathscr{L}^+(\alpha). \end{aligned}\right\} \tag{A 6}$$

The factorization $\gamma_2(\alpha)=\gamma_2^+(\alpha)\gamma_2^-(\alpha)$, with $\gamma_2^\pm(\alpha)$ analytic and non-zero in the upper/lower half-planes is a standard result. Note in (A 6) that the factors associated with the various Kelvin–Helmholtz modes have been put into the plus factor, since the Kelvin–Helmholtz modes all lie in the (deformed) lower half-plane. Note also that factor $\omega+\alpha M_2$ is also in the plus factor since the zero of $L(\alpha)$ at $\alpha=-\omega/M_2$ lies in the lower half-plane (this latter fact follows from considering ω to have a small positive imaginary part).

Our definition of $\mathscr{L}(\alpha)$ ensures that $\mathscr{L}^\pm(\alpha)\to 1$ as $\alpha\to\infty$ in the upper/lower-half-planes, and it is therefore easy to see from (A 1) that, for $M_2\neq 0$, $L^+\sim\alpha^{3/2}$ and $L^-\sim\alpha^{1/2}$ as α approaches infinity in the corresponding half-plane. In the special case $M_2=0$, we have $L^\pm\sim\alpha^{1/2}$ in the corresponding half-plane.

To factorize $\tilde{L}(\alpha)$ we write

$$\tilde{L}(\alpha)=-\left[\frac{D_2M_2^2+M_3^2(\beta_2/\beta_3)}{(\omega+\alpha M_2)\gamma_2}\right]\left[\frac{(\alpha-u_0)(\alpha-u_0^*)}{(\alpha-w_0)(\alpha-w_0^*)}\right]\tilde{\mathscr{L}}(\alpha), \tag{A 7}$$

where

$$\tilde{\mathscr{L}}(\alpha) \equiv \frac{1}{D_2 M_2^2 + M_3^2(\beta_2/\beta_3)} \left[\frac{(\alpha - w_0)(\alpha - w_0^*)}{(\alpha - u_0)(\alpha - u_0^*)(\alpha - v_0)(\alpha - v_0^*)}\right] \frac{k_{21}k_{12} - k_{11}k_{22}}{k_{11}\Delta}. \quad \text{(A 8)}$$

We can now proceed to factorize $\tilde{L}(\alpha)$ exactly as we did for $L(\alpha)$. It turns out that for $M_2 \neq 0$, $\tilde{L}^+ \sim \alpha^{-3/2}$ and $\tilde{L}^- \sim \alpha^{-1/2}$ as α approaches infinity in the corresponding half-plane, while for $M_2 = 0$ we have $\tilde{L}^\pm \sim \alpha^{-1/2}$.

Finally, the multiplicative factorization of $M(\alpha)$ and $\tilde{M}(\alpha)$ proceeds in exactly the same way as it did for $L(\alpha)$ and $\tilde{L}(\alpha)$ respectively. It follows that the split factors $M^\pm(\alpha)$ and $\tilde{M}^\pm(\alpha)$ have the same algebraic behaviour at infinity in the appropriate half-planes as $L^\pm(\alpha)$ and $\tilde{L}^\pm(\alpha)$ respectively.

Appendix B. The matrix elements $\hat{k}_{ij}^\pm$ for $d < 0$.

Following the procedure set out in § 3, the eight elements $\hat{k}_{ij}^\pm$ have been found as follows:

$$\hat{k}_{11}^+(\alpha) = \frac{1}{L^+(\alpha)} + \sum_{i=1}^{\infty} \frac{\hat{k}_{12}^-(\beta_i^-) R_i \exp(\mathrm{i}\beta_i^- d)}{L^-(\beta_i^-) L^+(\alpha)(\alpha - \beta_i^-)}, \quad \text{(B 1)}$$

$$\hat{k}_{12}^+(\alpha) = \frac{(\alpha - v_0)(\alpha - v_0^*)}{(\alpha - u_0)(\alpha - u_0^*)} \left\{ \tilde{L}^+(\alpha) + \frac{\exp(-\mathrm{i}\alpha d) k_{12} \hat{k}_{11}^+(\alpha)}{k_{11}} - \sum_{i=1}^{\infty} \frac{\exp(-\mathrm{i}\beta_i^+ d) \hat{k}_{11}^+(\beta_i^+) S_i \tilde{L}^+(\alpha)}{\tilde{L}^+(\beta_i^+)(\alpha - \beta_i^+)} \right\}, \quad \text{(B 2)}$$

$$\hat{k}_{21}^+(\alpha) = \frac{1}{L^+(\alpha)} + \sum_{i=1}^{\infty} \frac{\hat{k}_{22}^-(\beta_i^-) R_i \exp(\mathrm{i}\beta_i^- d)}{L^-(\beta_i^-) L^+(\alpha)(\alpha - \beta_i^-)}, \quad \text{(B 3)}$$

$$\hat{k}_{22}^+(\alpha) = \frac{(\alpha - v_0)(\alpha - v_0^*)}{(\alpha - u_0)(\alpha - u_0^*)} \left\{ -\tilde{L}^+(\alpha) + \frac{\exp(-\mathrm{i}\alpha d) k_{12} \hat{k}_{21}^+(\alpha)}{k_{11}} - \sum_{i=1}^{\infty} \frac{\exp(-\mathrm{i}\beta_i^+ d) \hat{k}_{21}^+(\beta_i^+) S_i \tilde{L}^+(\alpha)}{\tilde{L}^+(\beta_i^+)(\alpha - \beta_i^+)} \right\}, \quad \text{(B 4)}$$

$$\hat{k}_{11}^-(\alpha) = L^-(\alpha) + L^-(\alpha) \sum_{i=1}^{\infty} \frac{\hat{k}_{12}^-(\beta_i^-) R_i \exp(\mathrm{i}\beta_i^- d)}{L^-(\beta_i^-)(\alpha - \beta_i^-)} - \frac{\hat{k}_{12}^-(\alpha) k_{21} \exp(\mathrm{i}\alpha d)}{k_{11}}, \quad \text{(B 5)}$$

$$\hat{k}_{12}^-(\alpha) = \frac{1}{\tilde{L}^-(\alpha)} - \sum_{i=1}^{\infty} \frac{\hat{k}_{11}^+(\beta_i^+) S_i \exp(-\mathrm{i}\beta_i^+ d)}{\tilde{L}^+(\beta_i^+) \tilde{L}^-(\alpha)(\alpha - \beta_i^+)}, \quad \text{(B 6)}$$

$$\hat{k}_{21}^-(\alpha) = L^-(\alpha) + L^-(\alpha) \sum_{i=1}^{\infty} \frac{\hat{k}_{22}^-(\beta_i^-) R_i \exp(\mathrm{i}\beta_i^- d)}{L^-(\beta_i^-)(\alpha - \beta_i^-)} - \frac{\hat{k}_{22}^-(\alpha) k_{21} \exp(\mathrm{i}\alpha d)}{k_{11}}, \quad \text{(B 7)}$$

$$\hat{k}_{22}^-(\alpha) = -\frac{1}{\tilde{L}^-(\alpha)} - \sum_{i=1}^{\infty} \frac{\hat{k}_{21}^+(\beta_i^+) S_i \exp(-\mathrm{i}\beta_i^+ d)}{\tilde{L}^+(\beta_i^+) \tilde{L}^-(\alpha)(\alpha - \beta_i^+)}. \quad \text{(B 8)}$$

Appendix C. The matrix elements $\hat{k}_{ij}^{\pm}$ for $d > 0$.

The eight elements of $\hat{k}_{ij}^{\pm}$ for $d > 0$ are:

$$\hat{k}_{11}^{+}(\alpha) = \frac{(\alpha - u_0)(\alpha - u_0^*)}{(\alpha - v_0)(\alpha - v_0^*)} \left\{ -\tilde{M}^{+}(\alpha) + \frac{\exp(\mathrm{i}\alpha d) k_{21} \hat{k}_{12}^{+}(\alpha)}{k_{22}^{p}(\alpha)} - \sum_{i=1}^{\infty} \frac{\exp(\mathrm{i}\delta_i^{+} d) \hat{k}_{12}^{+}(\delta_i^{+}) S_i \tilde{M}^{+}(\alpha)}{\tilde{M}^{+}(\delta_i^{+})(\alpha - \delta_i^{+})} \right\}, \quad \text{(C 1)}$$

$$\hat{k}_{12}^{+}(\alpha) = \frac{1}{M^{+}(\alpha)} + \sum_{i=1}^{\infty} \frac{\hat{k}_{11}^{-}(\delta_i^{-}) R_i \exp(-\mathrm{i}\delta_i^{-} d)}{M^{-}(\delta_i^{-}) M^{+}(\alpha)(\alpha - \delta_i^{-})}, \quad \text{(C 2)}$$

$$\hat{k}_{21}^{+}(\alpha) = \frac{(\alpha - u_0)(\alpha - u_0^*)}{(\alpha - v_0)(\alpha - v_0^*)} \left\{ \tilde{M}^{+}(\alpha) + \frac{\exp(\mathrm{i}\alpha d) k_{21} \hat{k}_{22}^{+}(\alpha)}{k_{22}^{p}(\alpha)} - \sum_{i=1}^{\infty} \frac{\exp(\mathrm{i}\delta_i^{+} d) \hat{k}_{22}^{+}(\delta_i^{+}) S_i \tilde{M}^{+}(\alpha)}{\tilde{M}^{+}(\delta_i^{+})(\alpha - \delta_i^{+})} \right\}, \quad \text{(C 3)}$$

$$\hat{k}_{22}^{+}(\alpha) = \frac{1}{M^{+}(\alpha)} + \sum_{i=1}^{\infty} \frac{\hat{k}_{21}^{-}(\delta_i^{-}) R_i \exp(-\mathrm{i}\delta_i^{-} d)}{M^{-}(\delta_i^{-}) M^{+}(\alpha)(\alpha - \delta_i^{-})}, \quad \text{(C 4)}$$

$$\hat{k}_{11}^{-}(\alpha) = \frac{1}{\tilde{M}^{-}(\alpha)} + \sum_{i=1}^{\infty} \frac{\hat{k}_{12}^{+}(\delta_i^{+}) S_i \exp(\mathrm{i}\delta_i^{+} d)}{\tilde{M}^{+}(\delta_i^{+}) \tilde{M}^{-}(\alpha)(\alpha - \delta_i^{+})}, \quad \text{(C 5)}$$

$$\hat{k}_{12}^{-}(\alpha) = M^{-}(\alpha) + M^{-}(\alpha) \sum_{i=1}^{\infty} \frac{\hat{k}_{11}^{-}(\delta_i^{-}) R_i \exp(-\mathrm{i}\delta_i^{-} d)}{M^{-}(\delta_i^{+})(\alpha - \delta_i^{-})} - \frac{\hat{k}_{11}^{-}(\alpha) k_{12} \exp(-\mathrm{i}\alpha d)}{k_{22}^{p}(\alpha)}, \quad \text{(C 6)}$$

$$\hat{k}_{21}^{-}(\alpha) = -\frac{1}{\tilde{M}^{-}(\alpha)} + \sum_{i=1}^{\infty} \frac{\hat{k}_{22}^{+}(\delta_i^{-}) S_i \exp(\mathrm{i}\delta_i^{+} d)}{\tilde{M}^{+}(\delta_i^{+}) \tilde{M}^{-}(\alpha)(\alpha - \delta_i^{+})}, \quad \text{(C 7)}$$

$$\hat{k}_{22}^{-}(\alpha) = M^{-}(\alpha) + M^{-}(\alpha) \sum_{i=1}^{\infty} \frac{\hat{k}_{21}^{-}(\delta_i^{-}) R_i \exp(-\mathrm{i}\delta_i^{-} d)}{M^{-}(\delta_i^{-})(\alpha - \delta_i^{-})} - \frac{\hat{k}_{21}^{-}(\alpha) k_{12} \exp(-\mathrm{i}\alpha d)}{k_{22}^{p}(\alpha)}. \quad \text{(C 8)}$$

The matrix equation to be solved for the unknown $\hat{k}_{11}^{-}(\delta_i^{-})$ and $\hat{k}_{12}^{+}(\delta_i^{+})$ takes the form

$$\sum_{j=1}^{\infty} (\mathscr{Y} + \mathscr{M} \mathscr{X}^{-1} \mathscr{M}^{T})_{ij} A_j = 1 - \sum_{j=1}^{\infty} (\mathscr{M} \mathscr{X}^{-1})_{ij} \qquad (i = 1, 2, \ldots.) \quad \text{(C 9)}$$

with

$$B_i = \mathscr{X}_{ii}^{-1} + \sum_{j=1}^{\infty} (\mathscr{X}^{-1} \mathscr{M}^{T})_{ij} A_j. \quad \text{(C 10)}$$

Here

$$A_i = \frac{\hat{k}_{11}^{-}(\delta_i^{-}) \exp(-\mathrm{i}\delta_i^{-} d) R_i}{M^{-}(\delta_i^{-})}, \quad B_i = \frac{\hat{k}_{12}^{+}(\beta_i^{+}) \exp(\mathrm{i}\delta_i^{+} d) S_i}{\tilde{M}^{+}(\delta_i^{+})},$$

$$\mathscr{X} = \mathrm{diag} \frac{M^{+}(\delta_j^{+}) \tilde{M}^{+}(\delta_j^{+}) \exp(-\mathrm{i}\delta_j^{+} d)}{S_j}, \quad \mathscr{Y} = \mathrm{diag} \frac{M^{-}(\delta_j^{-}) \tilde{M}^{-}(\delta_j^{-}) \exp(\mathrm{i}\delta_j^{-} d)}{R_j}, \quad \text{(C 11)}$$

and $\mathscr{M} = 1/(\delta_j^+ - \delta_i^-)$. The quantities R_i, S_i are now the residues of k_{12}/k_{22}^p and k_{21}/k_{22}^p at $\alpha = \delta_i^{\mp}$ respectively. The matrix equation to be solved for the unknown $\hat{k}_{21}^-(\delta_i^-)$ and $\hat{k}_{22}^+(\delta_i^+)$ takes the form (C 9) but with the 1 on the right-hand side replaced by -1.

REFERENCES

Abrahams, I. D. 1987*a* Scattering of sound by three semi-infinite planes. *J. Sound Vib.* **112**, 396–398.

Abrahams, I. D. 1987*b* Scattering of sound by two parallel semi-infinite screens. *Wave Motion* **9**, 289–300.

Abrahams, I. D. 1997 On the solution of Wiener-Hopf problems involving noncommutative matrix kernel decompositions. *SIAM J. Appl. Maths* **57**, 541–567.

Abrahams, I. D. 2000 The application of Padé approximants to Wiener-Hopf factorization. *IMA J. Appl. Maths* **65**, 257–281.

Abrahams, I. D. 2002 On the application of the Wiener-Hopf technique to problems in dynamic elasticity. *Wave Motion* **36**, 311–333.

Abrahams, I. D. & Wickham, G. R. 1988 On the scattering of sound by two semi-infinite parallel staggered plates. I. explicit matrix Wiener-Hopf factorization. *Proc. R. Soc. Lond.* A **420**, 131–156.

Abrahams, I. D. & Wickham, G. R. 1990*a* Genertal Wiener-Hopf factorization of matrix kernels with exponential phase factors. *AIAM J. Appl. Maths* **50**, 819–838.

Abrahams, I. D. & Wickham, G. R. 1990*b* The scattering of sound by two semi-infinite parallel staggered plates. II. evaluation of the velocity potential for an incident plane wave and an incident duct mode. *Proc. R. Soc. Lond.* A **427**, 139–171.

Abramowitz, M. & Stegun, I. 1965 *Handbook of Mathematical Functions*. Dover.

Baker, G. A. & Graves-Morris, P. 1996 *Padé Approximants,* 2nd Edn. Cambridge University Press.

Brazier-Smith, P. R. & Scott, J. F. M. 1991 On the determination of the roots of dispersion equations by use of winding number integrals. *J. Sound Vib.* **145**, 503–510.

Cargill, A. M. 1982*a* Low frequency acoustic radiation from a jet pipe - a second order theory. *J. Sound Vib.* **83**, 339–354.

Cargill, A. M. 1982*b* Low-frequency sound radiation and generation due to the interaction of unsteady flow with a jet pipe. *J. Fluid Mech.* **121**, 59–105.

Cargill, A. M. 1982*c* The radiation of high-frequency sound out of a jet pipe. *J. Sound Vib.* **83**, 313–337.

Chapman, C. J. 1994 Sound radiation from a cylindrical duct. 1. ray structure of the duct modes and of the external field. *J. Fluid Mech.* **281**, 293–311.

Crighton, D. G. 1985 The Kutta condition in unsteady flow. *Annu. Rev. Fluid Mech.* **17**, 411–445.

Crighton, D. G. & Leppington, F. G. 1974 Radiation properties of the semi-infinite vortex sheet - the initial-value problem. *J. Fluid Mech.* **64**, 393–414.

Daniele, V. G. 1984 On the solution of two coupled Wiener-Hopf equations. *SIAM J. Appl. Maths* **44**, 667–680.

Demir, A. & Rienstra, S. W. 2006 Sound radiation from an annular duct with jet flow and a lined centerbody. *AIAA Paper* 2006–2718.

Demir, A. & Rienstra, S. W. 2007 Sound radiation from a buried nozzle with jet and bypass flow. In *Proc. Fourteenth Intl Congress on Sound and Vibration*, *ICSV14* 449. Cairns, Australia.

Gabard, G. & Astley, R. J. 2006 Theoretical model for sound radiation from annular jet pipes: far- and near-field solutions. *J. Fluid Mech.* **549**, 315–341.

Homicz, G. F. & Lordi, J. A. 1975 A note on the radiative directivity patterns of duct acoustic modes. *J. Sound Vib.* **41**, 283–290.

Idemen, M. 1979 A new method to obtain exact solutions of vector Wiener-Hopf equations. *Z. Angew. Math. Mech.* **59**, 656–659.

Jones, D. S. 1986 Diffraction by three semi-infinite planes. *Proc. R. Soc. Lond.* A **404**, 299–321.

Keith, G. M. & Peake, N. 2002 High-wavenumber acoustic radiation from a thin-walled axisymmetric cylinder. *J. Sound Vib.* **255**, 129–146.

KHRAPKOV, A. A. 1971*a* Certain cases of the elastic equilibrium of an infinite wedge with a nonsymmetric notch at the vertex, subjected to concentrated forces. *Prikl. Math. Mech.* **35**(4), 677–689.

KHRAPKOV, A. A. 1971*b* Closed form solutions of problems on the elastic equilibrium of an infinite wedge with nonsymmetric notch at the apex. *Prikl. Math. Mech.* **35** (6), 1062–1069.

LAWRIE, J. B. & ABRAHAMS, I. D. 1994 Acoustic radiation from two opposed semi-infinite coaxial cylindrical waveguides. II: separated ducts. *Wave Motion* **19**, 83–109.

LAWRIE, J. B., ABRAHAMS, I. D. & LINTON, C. M. 1993 Acoustic radiation from two opposed semi-infinite coaxial cylindrical waveguides. I: overlapping edges. *Wave Motion* **18**, 121–142.

LEVINE, H. & SCHWINGER, J. 1948 On the radiation of sound from an unflanged circular pipe. *Phys. Rev.* **73**, 383–406.

MUNT, R. 1977 The interaction of sound with a subsonic jet issuing from a semi-infinite cylinder. *J. Fluid Mech.* **83**, 609–640.

MUNT, R. 1990 Acoustic transmission properties of a jet pipe with subsonic jet flow: I. the cold jet reflection coefficient. *J. Sound Vib.* **142**, 413–436.

NOBLE, B. 1988 *Methods Based on the Wiener-Hopf Technique*. Chelsea.

OWEN, G. W. & ABRAHAMS, I. D. 2006 Elastic wave radiation from a high frequency finite-length transducer. *J. Sound Vib.* **298**, 108–131.

PLUMBLEE, H. E. & DEAN, P. D. 1973*a* Radiated sound field measurements from an annular flow duct facility. *J. Sound Vib.* **30**, 373–394.

PLUMBLEE, H. E. & DEAN, P. D. 1973*b* Sound measurements within and in the radiated field of an annular duct with flow. *J. Sound Vib.* **28**, 715–735.

RIENSTRA, S. W. 1983 A small Strouhal number analysis for acoustic wave-jet flow-pipe interaction. *J. Sound Vib.* **86**, 592–595.

RIENSTRA, S. W. 1984 Acoustic radiation from a semi-infinite annular duct in a uniform subsonic mean flow. *J. Sound Vib.* **94**, 267–288.

SAMANTA, A. & FREUND, J. B. 2008 Finite-wavelength scattering of incident vorticity waves at a shrouded exit. *J. Fluid Mech.* (in press).

TAYLOR, M. V., CRIGHTON, D. G. & CARGILL, A. M. 1993 The low frequency aeroacoustics of buried nozzle systems. *J. Sound Vib.* **163**, 493–526.

VEITCH, B. & PEAKE, N. 2007 Models for acoustic propagation through turbofan exhasut flows. *AIAA Paper* 2007-3543.